



# PHYSICAL-CONSTRAINT-PRESERVING CENTRAL DISCONTINUOUS GALERKIN METHODS FOR SPECIAL RELATIVISTIC HYDRODYNAMICS WITH A GENERAL EQUATION OF STATE

KAILIANG WU<sup>1</sup> AND HUAZHONG TANG<sup>2,3</sup>

<sup>1</sup> School of Mathematical Sciences, Peking University, Beijing 100871, P.R. China; [wukl@pku.edu.cn](mailto:wukl@pku.edu.cn)

<sup>2</sup> HEDPS, CAPT & LMAM, School of Mathematical Sciences, Peking University, Beijing 100871, P.R. China; [hztang@math.pku.edu.cn](mailto:hztang@math.pku.edu.cn)

<sup>3</sup> School of Mathematics and Computational Sciences, Xiangtan University, Xiangtan 411105, Hunan Province, P.R. China

Received 2016 July 28; revised 2016 November 7; accepted 2016 November 10; published 2016 December 27

## ABSTRACT

The ideal gas equation of state (EOS) with a constant adiabatic index is a poor approximation for most relativistic astrophysical flows, although it is commonly used in relativistic hydrodynamics (RHD). This paper develops high-order accurate, physical-constraints-preserving (PCP), central, discontinuous Galerkin (DG) methods for the one- and two-dimensional special RHD equations with a general EOS. It is built on our theoretical analysis of the admissible states for RHD and the PCP limiting procedure that enforce the admissibility of central DG solutions. The convexity, scaling invariance, orthogonal invariance, and Lax–Friedrichs splitting property of the admissible state set are first proved with the aid of its equivalent form. Then, the high-order central DG methods with the PCP limiting procedure and strong stability-preserving time discretization are proved, to preserve the positivity of the density, pressure, specific internal energy, and the bound of the fluid velocity, maintain high-order accuracy, and be  $L^1$ -stable. The accuracy, robustness, and effectiveness of the proposed methods are demonstrated by several 1D and 2D numerical examples involving large Lorentz factor, strong discontinuities, or low density/pressure, etc.

*Key words:* equation of state – hydrodynamics – methods: numerical – shock waves – relativistic processes

## 1. INTRODUCTION

In many cases, high-energy physics and astrophysics may involve fluid flows where the velocities are close to the speed of light, or the influence of large gravitational potentials cannot be ignored, such that the relativistic effect should be taken into account. Relativistic hydrodynamics (RHD) is important in investigating numerous astrophysical phenomena, from stellar to galactic scales; e.g., gamma-ray bursts, astrophysical jets, core collapse super-novae, coalescing neutron stars, formation of black holes, etc.

The RHD equations are highly nonlinear, making their analytical treatment extremely difficult. Numerical simulation has become a primary and powerful approach to understand the physical mechanisms of RHDs. Pioneering numerical work in this area may date back to the May and White finite difference code via artificial viscosity for the spherically symmetric general RHD equations in the Lagrangian coordinate (May & White 1966, 1967). Wilson first attempted to solve multi-dimensional RHD equations in the Eulerian coordinate by using the finite difference method with the artificial viscosity technique (Wilson 1972). Since the 1990s, the numerical study of the RHDs has attracted considerable attention, and various modern shock-capturing methods with an exact or approximate Riemann solver have been developed for RHD equations. The readers are referred to the early review articles (Martí & Müller 2003; Font 2008) and more recent works (Wu & Tang 2014, 2015, 2016), as well as references therein.

Most existing methods do not preserve the positivity of the density and pressure, as well as the specific internal energy and the bound of the fluid velocity at the same time, although they have been used to solve some RHD problems successfully. There exists a large risk of failure when a numerical scheme is applied to the RHD problems with large Lorentz factor, low density or pressure, or strong discontinuity, because as soon as the negative density or pressure, or the superluminal fluid velocity may be obtained, the eigenvalues of the Jacobian matrix become

imaginary, such that the discrete problem becomes ill-posed. It is of great significance to develop high-order accurate numerical schemes, whose solutions satisfy the intrinsic physical constraints. Recent years have witnessed some advances in developing high-order accurate bound-preserving type schemes for hyperbolic conservation laws. Those schemes are mainly built on two types of limiting procedures. One is the simple scaling limiting procedures for the reconstructed or evolved solution polynomials in a finite volume or discontinuous Galerkin (DG) method, (e.g., Xing et al. 2010; Zhang & Shu 2010a, 2010b, 2011a; Zhang et al. 2012). Another is the flux-corrected limiting procedure, which can be used on high-order finite difference, finite volume, and DG methods, (e.g., Hu et al. 2013; Jiang & Xu 2013; Liang & Xu 2014; Xu 2014; Christlieb et al. 2015; Xiong et al. 2016). A survey of the maximum-principle-satisfying or positivity-preserving high-order schemes based on the first-type limiter was presented in Zhang & Shu (2011b). The readers are also referred to Xu & Zhang (2016) for a review of those two approaches for enforcing the bound-preserving property in high order schemes. Two works were recently conducted to develop the physical-constraints-preserving (PCP) schemes for the special RHD equations with an ideal equation of state (EOS) by extending the above bound-preserving techniques. One is the high-order accurate PCP finite difference weighted essentially non-oscillatory (WENO) schemes proposed in Wu & Tang (2015), another is the bound preserving DG methods presented in (Qin et al. 2016). Recently, the extension of PCP schemes to the ideal relativistic magnetohydrodynamics was first studied in Wu & Tang (2016).

Although the ideal gas EOS with a constant adiabatic index is commonly used in RHD, it is a poor approximation for most relativistic astrophysical flows (e.g., Synge 1957; Falle & Komissarov 1996; Ryu et al. 2006; Choi & Wiita 2010). The aim of the paper is to study the properties of the admissible states and develop high-order accurate PCP central DG methods for the special RHD equations, with a general EOS. The central DG method was first introduced in Liu et al. (2007, 2008) for the

hyperbolic problems and well-developed for the Hamilton-Jacobi equations (Li & Yakovlev 2010), ideal magnetohydrodynamic equations (Li et al. 2011; Li & Xu 2012; Yakovlev et al. 2013), and RHD and magnetohydrodynamics (Zhao 2014; Zhao & Tang 2016a, 2016b), etc. Recently, positivity-preserving techniques for central DG method were discussed in Cheng et al. (2013) without rigorous proof for the ideal non-relativistic magnetohydrodynamics. The central DG methods evolve two approximate solutions on overlapping meshes, and do not need any exact or approximate Riemann solver across the cell interfaces, which is very complicated and time-consuming, especially for a general EOS. The central DG methods carry many features of non-central DG methods, and allow relatively larger time steps than non-central DG methods (Liu et al. 2008). Recently, they have become attractive and promising for magnetohydrodynamics, because of their easily achieving globally divergence-free numerical magnetic field (Li et al. 2011; Li & Xu 2012; Zhao & Tang 2016b). In comparison with the existing works in the non-relativistic or relativistic cases, it is a non-trivial task to develop a high-order accurate, provable PCP central DG method for the RHDs with general EOS. The technical challenge mainly comes from the inherent nonlinear coupling between the RHD equations due to the Lorentz factor and general EOS, no explicit expressions of the primitive variables and flux vectors with respect to the conservative vector, and one more physical constraint for the fluid velocity in addition to the positivity of the density, pressure, and specific internal energy.

The paper is organized as follows. Section 2 introduces the governing equations and the general EOS. Section 3 analyzes the admissible state set. Section 4 presents the high-order accurate PCP central DG methods for the 1D and 2D RHD equations with a general EOS. Section 5 gives several numerical examples to verify the accuracy, robustness, and effectiveness of the proposed methods for ultra-relativistic problems with large Lorentz factor, strong discontinuities, or low density or pressure, etc. Concluding remarks are presented in Section 6.

## 2. GOVERNING EQUATIONS

In the framework of special relativity, the ideal fluid flow is governed by the laws of particle number conservation and energy-momentum conservation (Landau & Lifshitz 1987). In the laboratory frame of reference, the  $d$ -dimensional special RHD equations may be written into a system of conservation laws as follows

$$\frac{\partial \mathbf{U}}{\partial t} + \sum_{i=1}^d \frac{\partial \mathbf{F}_i(\mathbf{U})}{\partial x_i} = 0, \quad (1)$$

where  $d = 1$ , or  $2$ , or  $3$ ,  $\mathbf{U} = (D, \mathbf{m}, E)^T$  denotes the conservative vector, and  $\mathbf{F}_i$  is the flux in the  $x_i$ -direction, which is defined by

$$\mathbf{F}_i = (Dv_i, v_i \mathbf{m} + p \mathbf{e}_i, m_i)^T, \quad i = 1, \dots, d. \quad (2)$$

Here, the mass density  $D = \rho W$ , the momentum density (row) vector  $\mathbf{m} = (m_1, \dots, m_d) = DhW\mathbf{v}$ , the energy density  $E = DhW - p$ , and  $\rho, \mathbf{v} = (v_1, \dots, v_d)$ , and  $p$  denote the rest-mass density, fluid velocity vector, and pressure, respectively. Moreover, the row vector  $\mathbf{e}_i$  denotes the  $i$ -th row of the identity matrix of order  $d$ ,  $W = 1/\sqrt{1 - v^2}$  is the Lorentz factor with  $v := (v_1^2 + \dots + v_d^2)^{1/2}$ , and  $h$  denotes the specific enthalpy

defined by

$$h = 1 + e + \frac{p}{\rho}, \quad (3)$$

with units in which the speed of light  $c$  is equal to one, and  $e$  is the specific internal energy.

An additional thermodynamic equation relating state variables, the so-called EOS, is needed to close the system (1). A general EOS may be expressed as

$$e = e(p, \rho), \quad (4)$$

or

$$h = h(p, \rho) = 1 + e(p, \rho) + p/\rho. \quad (5)$$

The relativistic kinetic theory reveals (Taub 1948) that the EOS (5) should satisfy

$$\left(h - \frac{p}{\rho}\right) \left(h - \frac{4p}{\rho}\right) \geq 1,$$

which implies a weaker inequality

$$h(p, \rho) \geq \sqrt{1 + p^2/\rho^2} + p/\rho. \quad (6)$$

It can also be derived from the kinetic theory (see Appendix A), and will be useful in analyzing the admissible state of RHD Equation (1).

For a general EOS, the local sound speed  $c_s$  is defined by

$$c_s^2 = \frac{1}{h} \frac{\partial p(\rho, S)}{\partial \rho} = \frac{1}{\frac{\partial p(p, S)}{\partial p} h}, \quad (7)$$

where the entropy  $S$  is related to other thermodynamic variables (Landau & Lifshitz 1987) by

$$TdS = de + pd\left(\frac{1}{\rho}\right) = dh - \frac{1}{\rho}dp, \quad (8)$$

where  $T$  denotes the thermodynamical temperature.

We will consider the causal EOS, i.e., those for which

$$0 < c_s < c = 1. \quad (9)$$

For such EOS, the hyperbolic property of (1) is preserved. The readers are referred to Zhao & Tang (2013) for the calculation of eigenvalues and (left and right) eigenvectors for the system (1) with  $d = 1$  and  $2$  and a general EOS.

**Lemma 2.1.** *If the fluid's coefficient of thermal expansion  $\beta = -\frac{\partial \ln \rho(T, p)}{\partial T} > 0$ , then the following inequality holds*

$$h \left( \frac{1}{\rho} - \frac{\partial h(p, \rho)}{\partial p} \right) < \frac{\partial h(p, \rho)}{\partial \rho} < 0. \quad (10)$$

**Proof.** Taking partial derivatives of  $e(p, \rho(T, p)) = e(T, \rho(T, p))$  with respect to  $T$  gives

$$\frac{\partial e(p, \rho)}{\partial \rho} \frac{\partial \rho(T, p)}{\partial T} = \frac{\partial e(T, \rho)}{\partial T} + \frac{\partial e(T, \rho)}{\partial \rho} \frac{\partial \rho(T, p)}{\partial T},$$

being equivalent to

$$\frac{\partial e(p, \rho)}{\partial \rho} \frac{\partial \rho(T, p)}{\partial T} = C_p + \frac{p}{\rho^2} \frac{\partial \rho(T, p)}{\partial T}, \quad (11)$$

where

$$C_p := \frac{\partial e(T, \rho)}{\partial T} + \left( \frac{\partial e(T, \rho)}{\partial \rho} - \frac{p}{\rho^2} \right) \frac{\partial \rho(T, p)}{\partial T} \in \mathbb{R}^+,$$

denotes the specific heat capacity at constant pressure. Using the definition of  $\beta$  and (11) gives

$$\frac{\partial e(p, \rho)}{\partial \rho} - \frac{p}{\rho^2} = -\frac{C_p}{\rho\beta} < 0.$$

Combining it with (5) yields

$$\frac{\partial h(p, \rho)}{\partial \rho} < 0. \quad (12)$$

Utilizing  $h = h(p, \rho) = h(p, \rho(p, S))$  and the chain rule of derivation gives

$$\begin{aligned} \frac{1}{\rho} \frac{\partial h(p, S)}{\partial p} &= \frac{\partial h(p, \rho)}{\partial p} + \frac{\partial h(p, \rho)}{\partial \rho} \frac{\partial \rho(p, S)}{\partial p} \\ &\stackrel{(7)}{=} \frac{\partial h(p, \rho)}{\partial p} + \frac{\partial h(p, \rho)}{\partial \rho} \frac{1}{hc_s^2}. \end{aligned}$$

It follows that

$$h \left( \frac{1}{\rho} - \frac{\partial h(p, \rho)}{\partial p} \right) / \left( \frac{\partial h(p, \rho)}{\partial \rho} \right) = \frac{1}{c_s^2} \stackrel{(2.9)}{>} 1, \quad (13)$$

which completes the proof by (12). ■

The hypothesis of Lemma 2.1 is valid for most of compressible fluids, e.g., the gasses.

Before ending this section, we give several special EOS. The most commonly used EOS, which is called the ideal EOS, is given by

$$h = 1 + \frac{\Gamma p}{(\Gamma - 1)\rho}, \quad (14)$$

where  $\Gamma$  denotes the adiabatic index. In general, the adiabatic index  $\Gamma$  is taken as 5/3 for mildly relativistic or sub-relativistic cases, and as 4/3 for ultra-relativistic cases where  $e \gg \rho$ . Although the EOS (14) is commonly used in RHDs, it is a poor approximation for most relativistic astrophysical flows. It is borrowed from non-relativistic thermodynamics and inconsistent with relativistic kinetic theory, see (Ryu et al. 2006). The EOS (14) is a reasonable approximation only if the gas is either strictly sub-relativistic or ultra-relativistic. When the gas is semi-relativistic or two-component, (14) is no longer correct.

Because the correct EOS for the relativistic perfect gas has been recognized as being important, several investigations with a more general EOS have been reported in numerical RHD. For the one-component perfect gasses, several general EOS have been used in the literature. For example, the first is (Mathews 1971; Mignone et al. 2005)

$$h = \frac{5p}{2\rho} + \sqrt{\frac{9p^2}{4\rho^2} + 1}, \quad (15)$$

and the second (Sokolov et al. 2001) is described as follows

$$h = \frac{2p}{\rho} + \sqrt{\frac{4p^2}{\rho^2} + 1}, \quad (16)$$

Recently, a new approximate EOS (Ryu et al. 2006) is given as follows

$$h = \frac{2(6p^2 + 4p\rho + \rho^2)}{\rho(3p + 2\rho)}, \quad (17)$$

It is not difficult to verify that, aside from conditions (6) and (10), the EOS (14)–(17) satisfy that  $e(p, \rho)$  is continuously differentiable in  $\mathbb{R}^+ \times \mathbb{R}^+$  and satisfies

$$\lim_{p \rightarrow 0^+} e(p, \rho) = 0, \quad \lim_{p \rightarrow +\infty} e(p, \rho) = +\infty, \quad (18)$$

for any fixed positive  $\rho$ .

### 3. ADMISSIBLE STATES

For the RHD Equation (1), it is very natural and intuitive to define the (physical) admissible states  $\mathcal{U}$ .

**Definition 3.1.** The set of admissible states of the RHD Equation (1) is defined by

$$\mathcal{G} := \{ \mathbf{U} = (D, \mathbf{m}, E)^T \mid \rho(\mathbf{U}) > 0, p(\mathbf{U}) > 0, e(\mathbf{U}) > 0, v(\mathbf{U}) < 1 \}. \quad (19)$$

Unfortunately, four conditions in (19) are much difficultly verified by the given value of the conservative vector  $\mathbf{U}$ , because there is no explicit expression for the transformation  $\mathbf{U} \mapsto (\rho, p, e, v)$ . This also indicates that it very difficult to study the properties of  $\mathcal{G}$  and develop the PCP schemes for the RHD Equation (1) with the EOS (4) or (5). In practice, if giving the value of  $\mathbf{U}$ , then one has to iteratively solve a nonlinear algebraic equation, e.g., an equation for the unknown pressure  $p$

$$\begin{aligned} E + p &= Dh(p, \rho^{[U]}(p))(1 - |\mathbf{m}|^2/(E + p)^2)^{-1/2}, \\ p &\in \mathbb{R}^+, \end{aligned} \quad (20)$$

where

$$\rho^{[U]}(p) := D\sqrt{1 - |\mathbf{m}|^2/(E + p)^2}.$$

Once the positive solution of the above equation is obtained, denoted by  $p(\mathbf{U})$ , other variables may be sequentially calculated by

$$\begin{aligned} v(\mathbf{U}) &= \frac{|\mathbf{m}|}{E + p(\mathbf{U})}, \quad \rho(\mathbf{U}) = D\sqrt{1 - v^2(\mathbf{U})}, \\ e(\mathbf{U}) &= e(p(\mathbf{U}), \rho(\mathbf{U})). \end{aligned} \quad (21)$$

For the ideal EOS (14) with  $\Gamma \in (1, 2]$ , it has been rigorously proved in Wu & Tang (2015) that the physical constraints in (19) are equivalent to two explicit constraints on conservative vector

$$D > 0, \quad q(\mathbf{U}) := E - \sqrt{D^2 + |\mathbf{m}|^2} > 0. \quad (22)$$

Actually, for a general EOS (5), they are still necessary for  $\mathbf{U} \in \mathcal{G}$ .

**Lemma 3.1.** Under condition (6), the admissible state  $\mathbf{U} \in \mathcal{G}$  must satisfy (22).

**Proof.** Because  $\rho$ ,  $p$ , and  $e$  are positive and  $0 \leq v < c = 1$ , it is easy to get the following inequalities

$$D = \frac{\rho}{\sqrt{1-v^2}} > 0,$$

$$E = \frac{\rho h}{1-v^2} - p > \rho h - p \stackrel{(3)}{=} \rho(1+e) > 0.$$

Using (6) further gives

$$\begin{aligned} E^2 - (D^2 + |m|^2) &= \left( \frac{\rho h}{1-v^2} - p \right)^2 - \frac{\rho^2}{1-v^2} - \left( \frac{\rho h v}{1-v^2} \right)^2 \\ &= \left( \frac{\rho h}{1-v^2} \right)^2 + p^2 - 2p \frac{\rho h}{1-v^2} \\ &\quad - \frac{\rho^2}{1-v^2} - \left( \frac{\rho h v}{1-v^2} \right)^2 \\ &= \frac{1}{1-v^2} [(\rho h - p)^2 - \rho^2 - p^2 v^2] \\ &\stackrel{v \leq 1}{\geq} \frac{1}{1-v^2} [\rho^2(1+e)^2 - \rho^2 - p^2] \stackrel{(2.6)}{>} 0. \end{aligned}$$

It follows that  $q(U) = E - \sqrt{D^2 + |m|^2} > 0$ . The proof is completed. ■

**Lemma 3.2.** If  $U = (D, m, E)^T$  satisfies (22) and  $e(p, \rho)$  is continuously differentiable in  $\mathbb{R}^+ \times \mathbb{R}^+$ , then  $U$  belongs to  $\mathcal{G}$  under the conditions (6), (10), and (18).

**Proof.** Consider the pressure function defined by

$$\begin{aligned} \Psi^{[U]}(p) &:= Dh(p, \rho^{[U]}(p)) \sqrt{1 - \frac{|m|^2}{(E+p)^2}} \\ &\quad - (E+p) \left( 1 - \frac{|m|^2}{(E+p)^2} \right), \quad p \in [0, +\infty), \end{aligned}$$

which is related to (20). Obviously, for given  $U$  satisfying (22),  $\Psi^{[U]}(p) \in C^1[0, +\infty)$  and its derivative satisfies

$$\begin{aligned} \frac{d\Psi^{[U]}(p)}{dp} &= D \left[ \frac{\partial h}{\partial p}(p, \rho^{[U]}(p)) \sqrt{1 - \frac{|m|^2}{(E+p)^2}} \right. \\ &\quad \left. + \frac{D|m|^2}{(E+p)^3} \frac{\partial h}{\partial \rho}(p, \rho^{[U]}(p)) \right] \\ &\quad + \frac{D|m|^2}{(E+p)^3} h(p, \rho^{[U]}(p)) \left( 1 - \frac{|m|^2}{(E+p)^2} \right)^{-\frac{1}{2}} \\ &\quad - \frac{|m|^2}{(E+p)^2} - 1 \stackrel{(10)}{>} D \left[ \sqrt{1 - \frac{|m|^2}{(E+p)^2}} \right. \\ &\quad \left. - \frac{D|m|^2 h(p, \rho^{[U]}(p))}{(E+p)^3} \right] \frac{\partial h}{\partial p}(p, \rho^{[U]}(p)) \\ &\quad + \frac{2D|m|^2}{(E+p)^3} h(p, \rho^{[U]}(p)) \left( 1 - \frac{|m|^2}{(E+p)^2} \right)^{-\frac{1}{2}} \\ &\quad - \frac{|m|^2}{(E+p)^2} - 1 =: \hat{\Psi}^{[U]}(p). \end{aligned} \tag{23}$$

Thanks to (3) and (18), one yields

$$\lim_{p \rightarrow 0^+} h(p, \rho^{[U]}(p)) = 1, \quad \lim_{p \rightarrow +\infty} e(p, \rho^{[U]}(p)) = +\infty,$$

which implies

$$\begin{aligned} \lim_{p \rightarrow 0^+} \Psi^{[U]}(p) &= D \sqrt{1 - \frac{|m|^2}{E^2}} + \frac{|m|^2}{E} - E \\ &= (D - \sqrt{E^2 - |m|^2}) \sqrt{1 - \frac{|m|^2}{E^2}} < 0, \\ \lim_{p \rightarrow +\infty} \Psi^{[U]}(p) &= \lim_{p \rightarrow +\infty} D[1 + e(p, \rho^{[U]}(p))] \\ &\quad \times \sqrt{1 - \frac{|m|^2}{(E+p)^2}} + \frac{|m|^2}{E+p} - E = +\infty. \end{aligned}$$

By the *intermediate value theorem*,  $\Psi^{[U]}(p)$  has at least one positive zero, that is to say, there exist at least one positive solution to the algebraic equation  $\Psi^{[U]}(p) = 0$  or (20).

The subsequent task is to prove the uniqueness of positive zero of  $\Psi^{[U]}(p)$ . Proof by contradiction is used here. Assume that  $\Psi^{[U]}(p)$  has more than one positive zeros and the smallest two are respectively denoted by  $p_1(U)$  and  $p_2(U)$  satisfying  $p_2(U) > p_1(U) > 0$ . Because the equation  $\Psi^{[U]}(p) = 0$  is equivalent to (20), one has the identity

$$Dh(p_i, \rho^{[U]}(p_i)) = (E + p_i) \sqrt{1 - \frac{|m|^2}{(E + p_i)^2}}, \quad i = 1, 2. \tag{24}$$

Combing such identity and the condition (22) gives  $h(p_i, \rho^{[U]}(p_i)) > 0$ , and further using (10) yields

$$\frac{\partial h}{\partial p}(p_i, \rho^{[U]}(p_i)) > \frac{1}{\rho^{[U]}(p_i)} > 0. \tag{25}$$

Combining (24)–(25) with (23) gives

$$\begin{aligned} \frac{d\Psi^{[U]}(p_i)}{dp} &> \hat{\Psi}^{[U]}(p_i) \stackrel{(24)}{=} D \left( 1 - \frac{|m|^2}{(E + p_i)^2} \right)^{\frac{3}{2}} \\ &\quad \times \frac{\partial h}{\partial p}(p_i, \rho^{[U]}(p_i)) + \frac{|m|^2}{(E + p_i)^2} - 1 \\ &\stackrel{(25)}{>} D \left( 1 - \frac{|m|^2}{(E + p_i)^2} \right)^{\frac{3}{2}} \frac{1}{\rho^{[U]}(p_i)} \\ &\quad + \frac{|m|^2}{(E + p_i)^2} - 1 = 0, \quad i = 1, 2. \end{aligned}$$

This indicates

$$\begin{aligned} \lim_{\delta p \rightarrow 0} \frac{\Psi^{[U]}(p_i + \delta p) - \Psi^{[U]}(p_i)}{\delta p} &= \frac{d\Psi^{[U]}(p_i)}{dp} > 0, \\ i &= 1, 2. \end{aligned}$$

By  $\Psi^{[U]}(p_i) = 0$  and the  $(\varepsilon, \delta)$ -definition of limit, for  $\varepsilon_i = \frac{1}{2} \frac{d\Psi^{[U]}(p_i)}{dp} > 0$ , there exists  $\delta_i > 0$  such that

$$\left| \frac{\Psi^{[U]}(p_i + \delta p)}{\delta p} - \frac{d\Psi^{[U]}(p_i)}{dp} \right| < \varepsilon_i, \quad \forall \delta p \in (-\delta_i, \delta_i),$$



which is equivalent to

$$\varepsilon_i < \frac{\Psi^{[U]}(p_i + \delta p)}{\delta p} < 3\varepsilon_i, \quad \forall \delta p \in (-\delta_0, \delta_0),$$

where  $\delta_0 = \min \left\{ \delta_1, \delta_2, \frac{p_2 - p_1}{2} \right\} > 0$ . Therefore, it holds that  $(p_1 + \frac{\delta_0}{2}, p_2 - \frac{\delta_0}{2}) \subset (p_1, p_2)$  and

$$\Psi^{[U]} \left( p_1 + \frac{\delta_0}{2} \right) > 0, \quad \Psi^{[U]} \left( p_2 - \frac{\delta_0}{2} \right) < 0.$$

Thanks to the *intermediate value theorem*,  $\Psi^{[U]}(p)$  has zero in the interval  $(p_1 + \frac{\delta_0}{2}, p_2 - \frac{\delta_0}{2})$ . This conflicts with the assumption that  $p_1$  and  $p_2$  are the smallest two positive zeros of  $\Psi^{[U]}(p)$ . Hence, the assumption does not hold and  $\Psi^{[U]}(p)$  has unique positive zero, denoted by  $p(U)$ . Substituting the positive pressure  $p(U)$  into (21) and using (22) gives

$$v(U) = \frac{|m|}{E + p(U)} < \frac{|m|}{E} < 1, \\ \rho(U) = D\sqrt{1 - v^2(U)} > 0.$$

For any  $p, \rho \in \mathbb{R}^+$ , utilizing (10) gives

$$\frac{\partial e(p, \rho)}{\partial p} > 0,$$

which implies

$$e(U) = e(p(U), \rho(U)) > \lim_{p \rightarrow 0^+} e(p, \rho(U)) \stackrel{(18)}{=} 0.$$

In conclusion,  $U \in \mathcal{G}$ . The proof is completed.  $\blacksquare$

**Remark 3.1.** Under the EOS conditions (6), (10), and (18), Lemmas 3.1 and 3.2 indicate that the admissible set  $\mathcal{G}$  is equivalent to the set

$$\hat{\mathcal{G}} := \{U = (D, \mathbf{m}, E)^T \mid D > 0, q(U) > 0\}. \quad (26)$$

In comparison with  $\mathcal{G}$ , two constraints in the set  $\hat{\mathcal{G}}$  are directly imposed on the conservative variables, such that they are very easy to be verified when the value of  $U$  is given. For that reason, the further discussion will always be performed under the conditions (6), (10) and (18).

With the help of the equivalence between  $\mathcal{G}$  and  $\hat{\mathcal{G}}$ , the convexity of admissible state set  $\mathcal{G}$  may be proved by exactly following the proof of Lemma 2.2 in Wu & Tang (2015).

**Lemma 3.3.** The function  $q(U)$  is concave and Lipschitz continuous with respect to  $U$ . The admissible set  $\hat{\mathcal{G}}$  is an open convex set. Moreover,  $\lambda U_1 + (1 - \lambda)U_0 \in \hat{\mathcal{G}}$  for any  $U_1 \in \hat{\mathcal{G}}$ ,  $U_0 \in \hat{\mathcal{G}} \cup \partial\hat{\mathcal{G}}$ , and  $\lambda \in (0, 1)$ .

By the convexity of  $\mathcal{G}$ , some properties of  $\mathcal{G}$  can be further obtained.

**Lemma 3.4.** If assuming  $U \in \mathcal{G}$ , then one has

- (i) (Scaling invariance)  $\lambda U \in \mathcal{G}$ , for all scalar  $\lambda > 0$ .
- (ii) (Orthogonal invariance)  $\mathbf{T}U \in \mathcal{G}$ , where  $\mathbf{T} = \text{diag} \{1, \mathbf{T}_d, 1\}$  and  $\mathbf{T}_d$  denotes any orthogonal matrix of size  $d$ .

- (iii) (Lax–Friedrichs splitting)  $U \pm c^{-1}F_i(U) \in \mathcal{G} \cup \partial\mathcal{G}$  and  $U \pm \alpha^{-1}F_i(U) \in \mathcal{G}$  for any  $\alpha > c = 1$ ,  $i = 1, \dots, d$ , where  $\partial\mathcal{G}$  denotes the boundary of  $\mathcal{G}$ .

**Proof.** The proof of the properties (i) and (ii) is direct and easy via the definition of  $\hat{\mathcal{G}}$  and omitted here. The following task is to prove the property (iii).

For any given  $i \in \{1, 2, \dots, d\}$ , if using  $D^\pm$ ,  $\mathbf{m}^\pm$ , and  $E^\pm$  to denote three components of the vector  $U \pm c^{-1}F_i(U)$ , then it is convenient to yield

$$D^\pm = D(1 \pm v_i) > 0, \\ E^\pm = E \pm m_i = (\rho h W^2 - p) \\ \pm \rho h W^2 v_i \geq \rho h W^2(1 - |v_i|) - p \\ \geq \frac{\rho h}{1 + v} - p > \frac{\rho h}{2} - p \stackrel{(6)}{\geq} \frac{1}{2}(\sqrt{\rho^2 + p^2} - p) > 0.$$

Further, using (6) gives

$$(D^\pm)^2 + |\mathbf{m}^\pm|^2 - (E^\pm)^2 \\ = (1 \pm v_i)^2 W^2 [\rho^2 + p^2 - (\rho + \rho e)^2] \leq 0.$$

It follows that  $q(U^\pm) \geq 0$ , and  $U \pm c^{-1}F_i(U) \in \hat{\mathcal{G}} \cup \partial\hat{\mathcal{G}}$ . On the other hand, for any  $\alpha > c = 1$ , using the convexity of  $\mathcal{G}$  and the above result gives

$$U \pm \alpha^{-1}F_i(U) = \left(1 - \frac{c}{\alpha}\right)U + \frac{c}{\alpha}U^\pm \in \hat{\mathcal{G}}.$$

The proof is completed.  $\blacksquare$

## 4. NUMERICAL METHODS

This section begins to develop PCP central DG methods for the 1D and 2D special RHD Equation (1).

### 4.1. 1D Case

For the sake of convenience, this subsection will use the symbol  $x$  to replace the independent variable  $x_1$  in (1). Let  $\{I_j := (x_{j-\frac{1}{2}}, x_{j+\frac{1}{2}})\}$  be a uniform partition of the 1D spatial domain  $\Omega$  with a constant spatial step-size  $\Delta x = x_{j+\frac{1}{2}} - x_{j-\frac{1}{2}}$ . With  $x_j = \frac{1}{2}(x_{j+\frac{1}{2}} + x_{j-\frac{1}{2}})$ , define a dual partition  $\{J_{j+\frac{1}{2}} := (x_j, x_{j+1})\}$ . The central DG methods seek two approximate solutions  $U_h^I(t, x)$  and  $U_h^J(t, x)$  on those mutually dual meshes  $\{I_j\}$  and  $\{J_{j+\frac{1}{2}}\}$ , where for each  $t \in (0, T_f]$ , each component of  $U_h^I$  (resp.  $U_h^J$ ) belongs to the finite dimensional space of discontinuous piecewise polynomial functions,  $\mathcal{V}_h^I$  (resp.  $\mathcal{V}_h^J$ ), defined by

$$\mathcal{V}_h^I := \{w(x) \in L^1(\Omega) \mid w(x)|_{I_j} \in \mathbb{P}^K(I_j)\}, \\ \mathcal{V}_h^J := \left\{w(x) \in L^1(\Omega) \mid w(x)|_{J_{j+\frac{1}{2}}} \in \mathbb{P}^K(J_{j+\frac{1}{2}})\right\},$$

where  $\mathbb{P}^K(I_j)$  and  $\mathbb{P}^K(J_{j+\frac{1}{2}})$  denote two spaces of polynomial of degree at most  $K$  on the cells  $I_j$  and  $J_{j+\frac{1}{2}}$ , respectively, and  $K$  is assumed to be a constant over the whole meshes.

Consider the central DG spatial discretization for  $U_h^I$ . Using a test function  $w(x) \in \mathbb{P}^K(I_j)$  to multiply (1) with  $d = 1$  and integrating by parts over the cell  $I_j$  give

$$\begin{aligned} \frac{d}{dt} \int_{I_j} U w dx &= \int_{I_j} F_1(U) \frac{dw}{dx} dx + F_1(U(t, x_{j-\frac{1}{2}})) \\ &\quad \times w(x_{j-\frac{1}{2}}) - F_1(U(t, x_{j+\frac{1}{2}})) w(x_{j+\frac{1}{2}}). \end{aligned} \quad (27)$$

Different from the standard DG discretization, the central DG discretization on the mesh  $\{I_j\}$  (resp.  $\{J_{j+\frac{1}{2}}\}$ ) use its dual solution  $U_h^J$  (resp.  $U_h^I$ ) to compute the volume and surface integrals related to the flux  $F$ . Specifically, replacing the exact solution  $U$  at the left- and right-hand sides of (27) with the approximate solutions  $U_h^I$  and  $U_h^J$ , respectively, gives

$$\begin{aligned} \frac{d}{dt} \int_{I_j} U_h^I w dx &= \frac{1}{\tau_{\max}} \int_{I_j} (U_h^J - U_h^I) w dx \\ &\quad + \int_{I_j} F_1(U_h^J) \frac{dw}{dx} dx \\ &\quad + F_1(U_h^J(t, x_{j-\frac{1}{2}})) w(x_{j-\frac{1}{2}}) \\ &\quad - F_1(U_h^J(t, x_{j+\frac{1}{2}})) w(x_{j+\frac{1}{2}}), \end{aligned} \quad (28)$$

where the first term on the right-hand side is an additional numerical dissipation term and important for the stability of central DG methods (Liu et al. 2008), and  $\tau_{\max}$  is the maximum time stepsize allowed by the CFL condition (Liu et al. 2007). The resulting central DG discretization (28) does not need numerical fluxes based on exact or approximate Riemann solvers, because the solutions or fluxes are evaluated at the cell interface  $x_{j\pm\frac{1}{2}}$ , i.e., the centers of dual cell  $J_{j\pm\frac{1}{2}}$ , where the solutions  $U_h^J$  are continuous. Due to the possible discontinuity of  $U_h^I$  at  $x = x_j$ , the second integration on the right-hand side of (28) is usually split into two parts

$$\begin{aligned} \int_{I_j} F_1(U_h^J) \frac{dw}{dx} dx &= \int_{x_{j-\frac{1}{2}}}^{x_j} F_1(U_h^J) \frac{dw}{dx} dx \\ &\quad + \int_{x_j}^{x_{j+\frac{1}{2}}} F_1(U_h^J) \frac{dw}{dx} dx, \end{aligned} \quad (29)$$

which may be evaluated approximately by numerical quadrature.

Let  $\{\Phi_j^{(\mu)}(x)\}_{\mu=0}^K$  denote a local orthogonal basis of the polynomial space  $\mathbb{P}^K(I_j)$ , and express the DG approximate solution  $U_h^I$  as

$$U_h^I(t, x) = \sum_{\mu=0}^K U_j^{I,(\mu)}(t) \Phi_j^{(\mu)}(x) =: U_j^I(t, x), \quad x \in I_j. \quad (30)$$

If substituting (30) into (28), taking the test function  $w(x) = \Phi_j^{(\nu)}(x)$ ,  $\nu = 0, 1, \dots, K$ , respectively, and applying a  $Q$ -point Gaussian quadrature to the integrations in (29), then the semi-discrete central DG discretization on the mesh  $\{I_j\}$  may be

reformed as follows

$$\begin{aligned} &\sum_{\mu=0}^K \left( \int_{I_j} \Phi_j^{(\mu)}(x) \Phi_j^{(\nu)}(x) dx \right) \frac{dU_j^{I,(\mu)}(t)}{dt} \\ &= \frac{1}{\tau_{\max}} \int_{I_j} (U_h^J - U_h^I) \Phi_j^{(\nu)}(x) dx \\ &\quad + \frac{\Delta x}{2} \sum_{\alpha=1}^Q \omega_{\alpha} \left( F_1(U_h^J(t, x_{j-\frac{1}{4}}^{\alpha})) \frac{d\Phi_j^{(\nu)}(x_{j-\frac{1}{4}}^{\alpha})}{dx} \right. \\ &\quad \left. + F_1(U_h^J(t, x_{j+\frac{1}{4}}^{\alpha})) \frac{d\Phi_j^{(\nu)}(x_{j+\frac{1}{4}}^{\alpha})}{dx} \right) \\ &\quad + F_1(U_h^J(t, x_{j-\frac{1}{2}})) \Phi_j^{(\nu)}(x_{j-\frac{1}{2}}) \\ &\quad - F_1(U_h^J(t, x_{j+\frac{1}{2}})) \Phi_j^{(\nu)}(x_{j+\frac{1}{2}}), \quad \nu = 0, \dots, K, \end{aligned} \quad (31)$$

where  $\{x_{j\pm\frac{1}{4}}^{\alpha}\}_{\alpha=1}^Q$  denotes the Gaussian nodes transformed into the interval  $[x_{j\pm\frac{1}{4}} - \frac{\Delta x}{4}, x_{j\pm\frac{1}{4}} + \frac{\Delta x}{4}]$ , and the associated Gaussian quadrature weights  $\{\omega_{\alpha}\}_{\alpha=1}^Q$  satisfy  $\omega_{\alpha} > 0$  and  $\sum_{\alpha=1}^Q \omega_{\alpha} = 1$ . For the accuracy requirement,  $Q$  should satisfy  $Q \geq K + 1$  for the  $\mathbb{P}^K$ -based DG methods (Cockburn et al. 1989).

The central DG spatial discretization for  $U_h^J$  is very similar. If using  $\{\Phi_{j+\frac{1}{2}}^{(\mu)}(x)\}_{\mu=0}^K$  to denote a local orthogonal basis of the polynomial space  $\mathbb{P}^K(J_{j+\frac{1}{2}})$ , and expressing the DG approximate solution  $U_h^J$  as

$$U_h^J(t, x) = \sum_{\mu=0}^K U_{j+\frac{1}{2}}^{J,(\mu)}(t) \Phi_{j+\frac{1}{2}}^{(\mu)}(x) =: U_{j+\frac{1}{2}}^J(t, x), \quad x \in J_{j+\frac{1}{2}}, \quad (32)$$

then the semi-discrete central DG discretization on the mesh  $\{J_{j+\frac{1}{2}}\}$  reads

$$\begin{aligned} &\sum_{\mu=0}^K \left( \int_{J_{j+\frac{1}{2}}} \Phi_{j+\frac{1}{2}}^{(\mu)}(x) \Phi_{j+\frac{1}{2}}^{(\nu)}(x) dx \right) \frac{dU_{j+\frac{1}{2}}^{J,(\mu)}(t)}{dt} \\ &= \frac{1}{\tau_{\max}} \int_{J_{j+\frac{1}{2}}} (U_h^I - U_h^J) \Phi_{j+\frac{1}{2}}^{(\nu)}(x) dx \\ &\quad + \frac{\Delta x}{2} \sum_{\alpha=1}^Q \omega_{\alpha} \left( F_1(U_h^I(t, x_{j+\frac{1}{4}}^{\alpha})) \frac{d\Phi_{j+\frac{1}{2}}^{(\nu)}(x_{j+\frac{1}{4}}^{\alpha})}{dx} \right. \\ &\quad \left. + F_1(U_h^I(t, x_{j+\frac{3}{4}}^{\alpha})) \frac{d\Phi_{j+\frac{1}{2}}^{(\nu)}(x_{j+\frac{3}{4}}^{\alpha})}{dx} \right) \\ &\quad + F_1(U_h^I(t, x_j)) \Phi_{j+\frac{1}{2}}^{(\nu)}(x_j) \\ &\quad - F_1(U_h^I(t, x_{j+1})) \Phi_{j+\frac{1}{2}}^{(\nu)}(x_{j+1}), \quad \nu = 0, \dots, K. \end{aligned} \quad (33)$$

If taking the bases as the scaled Legendre polynomials, e.g.,

$$\begin{aligned}\Phi_j^{(0)}(x) &= 1, \quad \Phi_j^{(1)}(x) = \frac{x - x_j}{\Delta x}, \\ \Phi_j^{(2)}(x) &= 12\left(\frac{x - x_j}{\Delta x}\right)^2 - 1, \dots, \quad \Phi_{j+\frac{1}{2}}^{(0)}(x) = 1, \\ \Phi_j^{(1)}(x) &= \frac{x - x_{j+\frac{1}{2}}}{\Delta x}, \quad \Phi_{j+\frac{1}{2}}^{(2)}(x) = 12\left(\frac{x - x_{j+\frac{1}{2}}}{\Delta x}\right)^2 - 1, \dots,\end{aligned}$$

then from (31) and (33) with  $\nu = 0$ , one may derive the evolution equations for the cell-averages of  $U_h^I$  and  $U_h^J$  as follows

$$\begin{aligned}\frac{dU_j^{I,(0)}(t)}{dt} &= \frac{1}{\Delta x} \left( \frac{1}{\tau_{\max}} \int_{I_j} (U_h^I - U_h^J) dx \right. \\ &\quad \left. + F_1(U_h^I(t, x_{j-\frac{1}{2}})) - F_1(U_h^I(t, x_{j+\frac{1}{2}})) \right) \\ &=: \mathcal{L}_j^I(U_h^I, U_h^J),\end{aligned}\quad (34)$$

and

$$\begin{aligned}\frac{dU_{j+\frac{1}{2}}^{J,(0)}(t)}{dt} &= \frac{1}{\Delta x} \left( \frac{1}{\tau_{\max}} \int_{J_{j+\frac{1}{2}}} (U_h^I - U_h^J) dx \right. \\ &\quad \left. + F_1(U_h^I(t, x_j)) - F_1(U_h^I(t, x_{j+1})) \right) \\ &=: \mathcal{L}_{j+\frac{1}{2}}^J(U_h^I, U_h^J).\end{aligned}\quad (35)$$

Equations (31) and (33) constitute a nonlinear system of ordinary differential equations for  $U_j^{I,(\mu)}(t)$  and  $U_{j+\frac{1}{2}}^{J,(\mu)}(t)$ , and may be rewritten into a compact form  $U'(t) = \mathcal{L}(U)$ . The strong stability preserving (SSP) Runge–Kutta methods or multi-step methods (Gottlieb et al. 2009) may be further taken for the time discretization in order to obtain the fully discrete central DG methods. For example, the third-order accurate SSP Runge–Kutta method

$$\begin{aligned}U^* &= U^n + \Delta t \mathcal{L}(U^n), \\ U^{**} &= \frac{3}{4}U^n + \frac{1}{4}(U^* + \Delta t \mathcal{L}(U^*)), \\ U^{n+1} &= \frac{1}{3}U^n + \frac{2}{3}(U^{**} + \Delta t \mathcal{L}(U^{**})),\end{aligned}\quad (36)$$

and the third-order accurate SSP multi-step method

$$\begin{aligned}U^{n+1} &= \frac{16}{27}(U^n + 3\Delta t \mathcal{L}(U^n)) \\ &\quad + \frac{11}{27}\left(U^{n-3} + \frac{12}{11}\Delta t \mathcal{L}(U^{n-3})\right),\end{aligned}\quad (37)$$

where  $\Delta t$  denotes the time stepsize in computations.

When  $K = 0$ , the above central DG methods reduce to corresponding first-order accurate central schemes on overlapping cells.

**Theorem 4.1.** *If  $K = 0$  and  $U_j^I, U_{j+\frac{1}{2}}^J \in \mathcal{G}$  for all  $j$ , then under the CFL type condition*

$$0 < \Delta t < \frac{\theta \Delta x}{2c}, \quad \theta := \frac{\Delta t}{\tau_{\max}} \in (0, 1], \quad (38)$$

one has

$$\begin{aligned}U_j^I + \Delta t \mathcal{L}_j^I(U_h^I, U_h^J) &\in \mathcal{G}, \\ U_{j+\frac{1}{2}}^J + \Delta t \mathcal{L}_{j+\frac{1}{2}}^J(U_h^I, U_h^J) &\in \mathcal{G},\end{aligned}$$

for all  $j$ .

**Proof.** Because both  $U_j^I$  and  $U_{j+\frac{1}{2}}^J$  are constant vectors when  $K = 0$ , one has

$$\begin{aligned}U_j^I + \Delta t \mathcal{L}_j^I(U_h^I, U_h^J) &= U_j^I + \frac{\Delta t}{\Delta x} \left( \frac{1}{\tau_{\max}} \int_{I_j} (U_h^I - U_h^J) dx \right. \\ &\quad \left. + F_1(U_{j-\frac{1}{2}}^J) - F_1(U_{j+\frac{1}{2}}^J) \right) \\ &= (1 - \theta)U_j^I + \frac{\theta}{2}(U_{j+\frac{1}{2}}^J + U_{j-\frac{1}{2}}^J) \\ &\quad + \frac{\Delta t}{\Delta x} (F_1(U_{j-\frac{1}{2}}^J) - F_1(U_{j+\frac{1}{2}}^J)) \\ &= (1 - \theta)U_j^I + \frac{\theta}{2}U_{j+\frac{1}{2}}^{J,-} + \frac{\theta}{2}U_{j-\frac{1}{2}}^{J,+},\end{aligned}\quad (39)$$

where

$$U_{j\pm\frac{1}{2}}^{J,\mp} := U_{j\pm\frac{1}{2}}^J \mp \left( \frac{\theta \Delta x}{2\Delta t} \right)^{-1} F_1(U_{j\pm\frac{1}{2}}^J).$$

Thanks to the Lax–Friedrichs splitting property in Lemma 3.4,  $U_{j\pm\frac{1}{2}}^{J,\mp} \in \mathcal{G}$  under the theorem hypothesis. Combing those with (39) and using the convexity of  $\mathcal{G}$  further yields  $U_j^I + \Delta t \mathcal{L}_j^I(U_h^I, U_h^J) \in \mathcal{G}$ . Similar arguments may show  $U_{j+\frac{1}{2}}^J + \Delta t \mathcal{L}_{j+\frac{1}{2}}^J(U_h^I, U_h^J) \in \mathcal{G}$ . The proof is completed.  $\blacksquare$

Theorem 4.1 indicates that the first-order accurate ( $K = 0$ ) central DG methods are PCP under the CFL type condition (38), if the forward Euler method is used for time discretization.

When  $K \geq 1$ , the high-order accurate central DG methods may work well for the 1D RHD problems whose solutions are either smooth or contain weak discontinuities and do not involve low density or pressure and a large Lorentz factor. However, if the solution contains strong discontinuity, the high-order accurate central DG methods will generate significant spurious oscillations and even nonlinear instability. Therefore, it is necessary to use some nonlinear limiter to suppress or control possible spurious oscillations. Up to now, there have existed some nonlinear limiters for the DG methods in the literature, e.g., the minmod-type limiter (Cockburn & Shu 1989), moment-based limiter (Biswas et al. 1994), WENO limiter (Qiu & Shu 2005; Zhu et al. 2008; Zhao & Tang 2013; Zhao 2014), and so on. Although those nonlinear limiters may effectively suppress spurious oscillations, they cannot make the high-order accurate central DG methods become PCP in general. To overcome such difficulty, the positivity-preserving limiters (Zhang & Shu 2010b; Cheng et al. 2013) will be extended to our central DG methods for the RHD equations: consider the scheme preserving the cell-averages  $U_j^{I,(0)}(t)$  and  $U_{j+\frac{1}{2}}^{J,(0)}(t)$  in  $\mathcal{G}$ , and then use those cell-averages to limit the

polynomial vector  $U_j^I(t, x)$  (resp.  $U_{j+\frac{1}{2}}^J(t, x)$ ) as  $\tilde{U}_j^I(t, x)$  (resp.  $\tilde{U}_{j+\frac{1}{2}}^J(t, x)$ ) such that the values of  $\tilde{U}_j^I(t, x)$  (resp.  $\tilde{U}_{j+\frac{1}{2}}^J(t, x)$ ) at some critical points in the cell  $I_j$  (resp.  $J_{j+\frac{1}{2}}$ ) belong to  $\mathcal{G}$ .

Before presenting the positivity-preserving limiter, the PCP conditions for the 1D high-order accurate central DG methods is first studied. For the sake of convenience, the independent variable  $t$  will be temporarily omitted. Let  $\{\hat{x}_{j\pm\frac{1}{4}}^\alpha\}_{\alpha=1}^L$  be the Gauss–Lobatto nodes transformed into the interval  $[x_{j\pm\frac{1}{4}} - \frac{\Delta x}{4}, x_{j\pm\frac{1}{4}} + \frac{\Delta x}{4}]$ , and  $\{\hat{\omega}_\alpha\}_{\alpha=1}^L$  be the associated Gaussian quadrature weights satisfying  $\hat{\omega}_\alpha > 0$  and  $\sum_{\alpha=1}^L \hat{\omega}_\alpha = 1$ , where  $L$  is larger than  $(K+3)/2$  in order to ensure that the algebraic precision of corresponding quadrature rule is at least  $K$ .

**Theorem 4.2.** *If  $U_j^I(\hat{x}_{j\pm\frac{1}{4}}^\alpha) \in \mathcal{G}$  and  $U_{j+\frac{1}{2}}^J(\hat{x}_{j+\frac{1}{2}\pm\frac{1}{4}}^\alpha) \in \mathcal{G}$  for all  $j$  and  $\alpha = 1, 2, \dots, L$ , then, under the CFL type condition,*

$$0 < \Delta t \leq \frac{\hat{\omega}_1 \theta \Delta x}{2c}, \quad \theta \in (0, 1], \quad (40)$$

one has

$$\begin{aligned} U_j^{I,(0)} + \Delta t \mathcal{L}_j^I(U_h^I, U_h^J) &\in \mathcal{G}, \\ U_{j+\frac{1}{2}}^{J,(0)} + \Delta t \mathcal{L}_{j+\frac{1}{2}}^J(U_h^I, U_h^J) &\in \mathcal{G}, \end{aligned}$$

for all  $j$ .

**Proof.** Using the convexity of  $\mathcal{G}$  and the exactness of the Gauss–Lobatto quadrature rule with  $L$  nodes for the polynomials of degree  $K$  yields

$$\begin{aligned} U_j^{I,(0)} &= \frac{1}{\Delta x} \int_{I_j} U_h^I dx \\ &= \frac{1}{2} \sum_{\alpha=1}^L \hat{\omega}_\alpha \left( U_j^I(\hat{x}_{j-\frac{1}{4}}^\alpha) + U_j^I(\hat{x}_{j+\frac{1}{4}}^\alpha) \right) \in \mathcal{G}, \end{aligned}$$

and

$$\begin{aligned} &\frac{1}{\Delta x} \int_{I_j} U_h^J dx \\ &= \frac{1}{2} \sum_{\alpha=1}^L \hat{\omega}_\alpha \left( U_{j-\frac{1}{2}}^J(\hat{x}_{j-\frac{1}{4}}^\alpha) + U_{j+\frac{1}{2}}^J(\hat{x}_{j+\frac{1}{4}}^\alpha) \right) \\ &= \frac{\hat{\omega}_1}{2} U_{j-\frac{1}{2}}^J(x_{j-\frac{1}{2}}) + \frac{\hat{\omega}_L}{2} U_{j+\frac{1}{2}}^J(x_{j+\frac{1}{2}}) \\ &\quad + \frac{1}{2} \sum_{\alpha=2}^L \hat{\omega}_\alpha U_{j-\frac{1}{2}}^J(\hat{x}_{j-\frac{1}{4}}^\alpha) \\ &\quad + \frac{1}{2} \sum_{\alpha=L-1}^L \hat{\omega}_\alpha U_{j+\frac{1}{2}}^J(\hat{x}_{j+\frac{1}{4}}^\alpha) \\ &= \frac{\hat{\omega}_1}{2} U_{j-\frac{1}{2}}^J(x_{j-\frac{1}{2}}) + \frac{\hat{\omega}_1}{2} U_{j+\frac{1}{2}}^J(x_{j+\frac{1}{2}}) + (1 - \hat{\omega}_1) \Xi, \end{aligned}$$

with

$$\begin{aligned} \Xi &:= \frac{1}{2(1 - \hat{\omega}_1)} \left( \sum_{\alpha=2}^L \hat{\omega}_\alpha U_{j-\frac{1}{2}}^J(\hat{x}_{j-\frac{1}{4}}^\alpha) \right. \\ &\quad \left. + \sum_{\alpha=1}^{L-1} \hat{\omega}_\alpha U_{j+\frac{1}{2}}^J(\hat{x}_{j+\frac{1}{4}}^\alpha) \right) \in \mathcal{G}, \end{aligned}$$

where  $\hat{\omega}_1 = \hat{\omega}_L = \frac{1}{2}$ . Thus, one has

$$\begin{aligned} U_j^{I,(0)} + \Delta t \mathcal{L}_j^I(U_h^I, U_h^J) &= U_j^{I,(0)} + \frac{\theta}{\Delta x} \int_{I_j} (U_h^J - U_j^I) dx \\ &\quad + \frac{\Delta t}{\Delta x} \left( F_1 \left( U_{j-\frac{1}{2}}^J(x_{j-\frac{1}{2}}) \right) - F_1 \left( U_{j+\frac{1}{2}}^J(x_{j+\frac{1}{2}}) \right) \right) \\ &= (1 - \theta) U_j^{I,(0)} + \theta \left( \frac{\hat{\omega}_1}{2} U_{j-\frac{1}{2}}^J(x_{j-\frac{1}{2}}) \right. \\ &\quad \left. + \frac{\hat{\omega}_1}{2} U_{j+\frac{1}{2}}^J(x_{j+\frac{1}{2}}) + (1 - \hat{\omega}_1) \Xi \right) \\ &\quad + \frac{\Delta t}{\Delta x} \left( F_1 \left( U_{j-\frac{1}{2}}^J(x_{j-\frac{1}{2}}) \right) - F_1 \left( U_{j+\frac{1}{2}}^J(x_{j+\frac{1}{2}}) \right) \right) \\ &= (1 - \theta) U_j^{I,(0)} + (1 - \hat{\omega}_1) \theta \Xi + \frac{\hat{\omega}_1 \theta}{2} U_{j+\frac{1}{2}}^{J,-} + \frac{\hat{\omega}_1 \theta}{2} U_{j-\frac{1}{2}}^{J,+}, \end{aligned} \quad (41)$$

where

$$\begin{aligned} U_{j\pm\frac{1}{2}}^{J,\mp} &:= U_{j\pm\frac{1}{2}}^J(x_{j\pm\frac{1}{2}}) \mp \left( \frac{\hat{\omega}_1 \theta \Delta x}{2 \Delta t} \right)^{-1} \\ &\quad \times F_1 \left( U_{j\pm\frac{1}{2}}^J(x_{j\pm\frac{1}{2}}) \right) \in \mathcal{G} \cup \partial \mathcal{G}, \end{aligned}$$

due to the Lax–Friedrichs splitting property in Lemma 3.4 and the theorem hypothesis. Using (41) and the convexity of  $\mathcal{G}$  may further yield  $U_j^{I,(0)} + \Delta t \mathcal{L}_j^I(U_h^I, U_h^J) \in \mathcal{G}$ . Similar arguments may show  $U_{j+\frac{1}{2}}^{J,(0)} + \Delta t \mathcal{L}_{j+\frac{1}{2}}^J(U_h^I, U_h^J) \in \mathcal{G}$ . The proof is completed.  $\blacksquare$

Theorem 4.2 gives a sufficient condition for the 1D central DG methods which preserve the cell-averages  $U_j^{I,(0)}$  and  $U_{j+\frac{1}{2}}^{J,(0)}$  in  $\mathcal{G}$  when the forward Euler method is used for the time discretization. Because a high-order accurate SSP time discretization may be considered as a convex combination of the forward Euler method, Theorem 4.2 is valid for the high-order accurate SSP time discretization.

Let us present the PCP limiting procedure, which limits  $U_j^I(x)$  and  $U_{j+\frac{1}{2}}^J(x)$  as  $\tilde{U}_j^I(x)$  and  $\tilde{U}_{j+\frac{1}{2}}^J(x)$  satisfying two requirements: (i)  $\tilde{U}_j^I(\hat{x}_{j\pm\frac{1}{4}}^\alpha) \in \mathcal{G}$  and  $\tilde{U}_{j+\frac{1}{2}}^J(\hat{x}_{j+\frac{1}{2}\pm\frac{1}{4}}^\alpha) \in \mathcal{G}$  for  $\alpha = 1, 2, \dots, L$ , and (ii)  $\tilde{U}_j^I(x_{j\pm\frac{1}{2}}^\alpha) \in \mathcal{G}$  and  $\tilde{U}_{j+\frac{1}{2}}^J(x_{j+\frac{1}{2}\pm\frac{1}{4}}^\alpha) \in \mathcal{G}$  for  $\alpha = 1, 2, \dots, Q$ . The second requirement does not appear in the non-relativistic case, and is used to ensure getting a physical solution of the pressure Equation (20) by root-finding method and the successive calculations of  $F_1 \left( U_j^I(x_{j\pm\frac{1}{4}}^\alpha) \right)$  and  $F_1 \left( U_{j+\frac{1}{2}}^J(x_{j+\frac{1}{2}\pm\frac{1}{4}}^\alpha) \right)$  in (31) and (33). Because the PCP limiting procedures for  $U_j^I(x)$  and  $U_{j+\frac{1}{2}}^J(x)$  are the same and implemented separately, only the PCP limiter for  $U_j^I(x)$  is



presented here. Let  $\mathbf{U}_j^I(x) := (D_j(x), \mathbf{m}_j(x), E_j(x))^T$ , assume that  $\mathbf{U}_j^{I,(0)} := (\bar{D}_j, \bar{\mathbf{m}}_j, \bar{E}_j)^T \in \mathcal{G}$ , and introduce a sufficiently small positive number  $\epsilon$  (taken as  $10^{-13}$  in numerical computations) such that  $\mathbf{U}_j^{I,(0)} \in \mathcal{G}_\epsilon$ , where

$$\mathcal{G}_\epsilon = \{\mathbf{U} = (D, \mathbf{m}, E)^T | D \geq \epsilon, q(\mathbf{U}) \geq \epsilon\}$$

Obviously,  $\mathcal{G}_\epsilon \subset \mathcal{G}_0$  and  $\lim_{\epsilon \rightarrow 0^+} \mathcal{G}_\epsilon = \mathcal{G}_0$ .

The 1D PCP limiting procedure is divided into the following two steps.

Step (i): enforce the positivity of  $D(\mathbf{U})$ . Let  $D_{\min} = \min_{x \in \mathcal{S}_j} D_j(x)$ , where

$$\mathcal{S}_j := \left\{ \hat{x}_{j-\frac{1}{4}}^\alpha \right\}_{\alpha=1}^L \cup \left\{ \hat{x}_{j+\frac{1}{4}}^\alpha \right\}_{\alpha=1}^L \cup \left\{ x_{j-\frac{1}{4}}^\alpha \right\}_{\alpha=1}^Q \cup \left\{ x_{j+\frac{1}{4}}^\alpha \right\}_{\alpha=1}^Q.$$

If  $D_{\min} < \epsilon$ , then  $D_j(x)$  is limited as

$$\hat{D}_j(x) = \theta_1(D_j(x) - \bar{D}_j) + \bar{D}_j,$$

where  $\theta_1 = (\bar{D}_j - \epsilon)/(\bar{D}_j - D_{\min}) < 1$ . Otherwise, take  $\hat{D}_j(x) = D_j(x)$  and  $\theta_1 = 1$ . Denote  $\hat{\mathbf{U}}_j(x) := (\hat{D}_j(x), \mathbf{m}_j(x), E_j(x))^T$ .

Step (ii): enforce the positivity of  $q(\mathbf{U})$ . Let  $q_{\min} = \min_{x \in \mathcal{S}_j} q(\hat{\mathbf{U}}_j(x))$ . If  $q_{\min} < \epsilon$ , then  $\hat{\mathbf{U}}_j(x)$  is limited as

$$\tilde{\mathbf{U}}_j^I(x) = \theta_2(\hat{\mathbf{U}}_j(x) - \mathbf{U}_j^{I,(0)}) + \mathbf{U}_j^{I,(0)},$$

where  $\theta_2 = (q(\mathbf{U}_j^{I,(0)}) - \epsilon)/(q(\mathbf{U}_j^{I,(0)}) - q_{\min}) < 1$ . Otherwise, set  $\tilde{\mathbf{U}}_j^I(x) = \hat{\mathbf{U}}_j(x)$  and  $\theta_2 = 1$ .

**Lemma 4.1.** *If  $\mathbf{U}_j^{I,(0)} \in \mathcal{G}_\epsilon$ , then  $\tilde{\mathbf{U}}_j^I(x)$ , given by the above PCP limiting procedure, belongs to  $\mathcal{G}_\epsilon$  for all  $x \in \mathcal{S}_j$ .*

**Proof.** For any  $x \in \mathcal{S}_j$ , it is obvious that  $\hat{D}_j(x) = D_j(x) \geq D_{\min} > \epsilon$  if  $D_{\min} > \epsilon$ . If  $D_{\min} < \epsilon$ , then one has

$$\hat{D}_j(x) = \theta_1(D_j(x) - \bar{D}_j) + \bar{D}_j \geq \theta_1(D_{\min} - \bar{D}_j) + \bar{D}_j = \epsilon.$$

Thanks to  $\theta_2 \in [0, 1]$ , one yields

$$\bar{D}_j^I(x) = \theta_2(\hat{D}_j(x) - \bar{D}_j) + \bar{D}_j \geq \theta_2(\epsilon - \bar{D}_j) + \bar{D}_j \geq \epsilon.$$

Similarly, if  $q_{\min} \geq \epsilon$ , then it is evident that  $q(\tilde{\mathbf{U}}_j^I(x)) = q(\hat{\mathbf{U}}_j(x)) \geq q_{\min} \geq \epsilon$  for any  $x \in \mathcal{S}_j$ . Otherwise, using the concavity of  $q(\mathbf{U})$  gives

$$\begin{aligned} q(\tilde{\mathbf{U}}_j^I(x)) &= q(\theta_2 \hat{\mathbf{U}}_j(x) + (1 - \theta_2) \mathbf{U}_j^{I,(0)}) \\ &\geq \theta_2 q(\hat{\mathbf{U}}_j(x)) + (1 - \theta_2) q(\mathbf{U}_j^{I,(0)}) \\ &\geq \theta_2 q_{\min} + (1 - \theta_2) q(\mathbf{U}_j^{I,(0)}) = \epsilon. \end{aligned}$$

The proof is completed.  $\blacksquare$

The above PCP limiting procedure preserves the conservation, in the sense that

$$\begin{aligned} \mathbf{U}_j^{I,(0)} &= \frac{1}{\Delta x} \int_{I_j} \mathbf{U}_j^I(x) dx \\ &= \frac{1}{\Delta x} \int_{I_j} \tilde{\mathbf{U}}_j^I(x) dx = \frac{1}{\Delta x} \int_{I_j} \tilde{\mathbf{U}}_j^I(x) dx, \end{aligned}$$

and maintains the high-order accuracy for smooth solutions, similar to the discussion at the end of Section 2.2 of Zhang & Shu (2010b). If replacing the solution polynomials  $\mathbf{U}_j^I(x)$  and  $\mathbf{U}_{j+\frac{1}{2}}^J(x)$  of high-order accurate central DG methods with the limited polynomials  $\tilde{\mathbf{U}}_j^I(x)$  and  $\tilde{\mathbf{U}}_{j+\frac{1}{2}}^J(x)$  at each stage of SSP Runge–Kutta method (36) or each step of SSP multi-step method (37), then the resulting fully discrete central DG methods are PCP under some CFL type conditions.

**Theorem 4.3.** *If the high-order accurate central DG solution polynomials are revised as the above limited polynomials at each stage of SSP Runge–Kutta method (36) or each step of SSP multi-step method (37), then (i) the resulting Runge–Kutta central DG methods are PCP under the CFL type condition (40), (ii) the resulting multi-step central DG methods are PCP under the CFL type condition*

$$0 < \Delta t \leq \frac{\hat{\omega}_1 \theta \Delta x}{2c}, \quad \theta \in \left(0, \frac{1}{3}\right]. \quad (42)$$

Similar to Wang et al. (2012), Cheng et al. (2013), and Qin et al. (2016), one may yield the  $L^1$ -stability of the proposed PCP central DG methods.

**Theorem 4.4.** *Under the vanishing, reflective, or periodic boundary conditions, the PCP central DG methods are  $L^1$ -stable in the sense that*

$$\begin{aligned} \|\tilde{\mathbf{U}}_h^I(t_n, x)\|_{L^1} + \|\tilde{\mathbf{U}}_h^J(t_n, x)\|_{L^1} \\ < 2(\|\mathbf{U}_h^I(0, x)\|_{L^1} + \|\mathbf{U}_h^J(0, x)\|_{L^1}), \end{aligned}$$

where

$$\begin{aligned} \|\mathbf{w}^I\|_{L^1} &:= \frac{\Delta x}{2} \sum_j \sum_{\alpha=1}^L \hat{\omega}_\alpha \left( \left\| \mathbf{w}_j^I(\hat{x}_{j-\frac{1}{4}}^\alpha) \right\|_{l^1} \right. \\ &\quad \left. + \left\| \mathbf{w}_j^I(\hat{x}_{j+\frac{1}{4}}^\alpha) \right\|_{l^1} \right) \approx \int_\Omega \|\mathbf{w}^I(x)\|_{l^1} dx, \end{aligned}$$

and

$$\begin{aligned} \|\mathbf{w}^J\|_{L^1} &:= \frac{\Delta x}{2} \sum_j \sum_{\alpha=1}^L \hat{\omega}_\alpha \left( \left\| \mathbf{w}_{j+\frac{1}{2}}^J(\hat{x}_{j+\frac{1}{4}}^\alpha) \right\|_{l^1} \right. \\ &\quad \left. + \left\| \mathbf{w}_{j+\frac{1}{2}}^J(\hat{x}_{j+\frac{3}{4}}^\alpha) \right\|_{l^1} \right) \approx \int_\Omega \|\mathbf{w}^J(x)\|_{l^1} dx. \end{aligned}$$

**Proof.** It only needs to consider the forward Euler time discretization. Because  $\tilde{D}_j^I(t_n, \hat{x}_{j\pm\frac{1}{4}}^\alpha)$  are larger than zero and the central DG methods are conservative, one yields

$$\begin{aligned}
\|\tilde{D}_h^I(t_n, x)\|_{L^1} &= \frac{\Delta x}{2} \sum_j \sum_{\alpha=1}^L \hat{\omega}_\alpha \left( \left| \tilde{D}_j^I(t_n, \hat{x}_{j-\frac{1}{4}}^\alpha) \right| \right. \\
&\quad \left. + \left| \tilde{D}_j^I(t_n, \hat{x}_{j+\frac{1}{4}}^\alpha) \right| \right) \\
&= \frac{\Delta x}{2} \sum_j \sum_{\alpha=1}^L \hat{\omega}_\alpha \left( \tilde{D}_j^I(t_n, \hat{x}_{j-\frac{1}{4}}^\alpha) + \tilde{D}_j^I(t_n, \hat{x}_{j+\frac{1}{4}}^\alpha) \right) \\
&= \sum_j \int_{I_j} \tilde{D}_j^I(t_n, x) dx = \sum_j \int_{I_j} D_j^I(t_n, x) dx \\
&= \Delta x \sum_j D_j^{I,(0)}(t_n) \\
&= \Delta x \sum_j (D_j^{I,(0)}(t_{n-1}) + \Delta t \mathcal{L}_j^{I,D}(\tilde{U}_h^I(t_{n-1}, x), \\
&\quad \tilde{U}_h^J(t_{n-1}, x))) \\
&= \sum_j \left( \Delta x \tilde{D}_j^{I,(0)}(t_{n-1}) + \theta \int_{I_j} (\tilde{D}_h^J(t_{n-1}, x) \right. \\
&\quad \left. - \tilde{D}_j^I(t_{n-1}, x)) dx \right) \\
&= (1 - \theta) \|\tilde{D}_h^I(t_{n-1}, x)\|_{L^1} \\
&\quad + \theta \|\tilde{D}_h^J(t_{n-1}, x)\|_{L^1}, \tag{43}
\end{aligned}$$

where  $\mathcal{L}_j^{I,D}$  denotes the first component of  $\mathcal{L}_j^I$ . Similarly, one has

$$\begin{aligned}
\|\tilde{D}_h^J(t_n, x)\|_{L^1} &= (1 - \theta) \|\tilde{D}_h^J(t_{n-1}, x)\|_{L^1} \\
&\quad + \theta \|\tilde{D}_h^I(t_{n-1}, x)\|_{L^1}. \tag{44}
\end{aligned}$$

Combining (43) with (44) gives

$$\begin{aligned}
&\|\tilde{D}_h^I(t_n, x)\|_{L^1} + \|\tilde{D}_h^J(t_n, x)\|_{L^1} \\
&= \|\tilde{D}_h^I(t_{n-1}, x)\|_{L^1} + \|\tilde{D}_h^J(t_{n-1}, x)\|_{L^1} \\
&= \dots = \|\tilde{D}_h^I(0, x)\|_{L^1} + \|\tilde{D}_h^J(0, x)\|_{L^1} \\
&= \|D_h^I(0, x)\|_{L^1} + \|D_h^J(0, x)\|_{L^1}.
\end{aligned}$$

Similar argument may get

$$\begin{aligned}
&\|\tilde{E}_h^I(t_n, x)\|_{L^1} + \|\tilde{E}_h^J(t_n, x)\|_{L^1} \\
&= \|\tilde{E}_h^I(t_{n-1}, x)\|_{L^1} + \|\tilde{E}_h^J(t_{n-1}, x)\|_{L^1} \\
&= \dots = \|E_h^I(0, x)\|_{L^1} + \|E_h^J(0, x)\|_{L^1}.
\end{aligned}$$

Using  $q(\tilde{U}_j^I(t_n, \hat{x}_{j\pm\frac{1}{4}}^\alpha)) > 0$  gives

$$\left| (\tilde{m}_1)_j^I(t_n, \hat{x}_{j\pm\frac{1}{4}}^\alpha) \right| < \tilde{E}_j^I(t_n, \hat{x}_{j\pm\frac{1}{4}}^\alpha),$$

thus one has

$$\|(\tilde{m}_1)_h^I(t_n, x)\|_{L^1} < \|\tilde{E}_h^I(t_n, x)\|_{L^1}.$$

Similarly, one also has

$$\|(\tilde{m}_1)_h^J(t_n, x)\|_{L^1} < \|\tilde{E}_h^J(t_n, x)\|_{L^1}.$$

Therefore one has

$$\begin{aligned}
&\|\tilde{U}_h^I(t_n, x)\|_{L^1} + \|\tilde{U}_h^J(t_n, x)\|_{L^1} \\
&< \|\tilde{D}_h^I(t_n, x)\|_{L^1} + \|\tilde{D}_h^J(t_n, x)\|_{L^1} \\
&\quad + 2(\|\tilde{E}_h^I(t_n, x)\|_{L^1} + \|\tilde{E}_h^J(t_n, x)\|_{L^1}) \\
&= \|D_h^I(0, x)\|_{L^1} + \|D_h^J(0, x)\|_{L^1} \\
&\quad + 2(\|E_h^I(0, x)\|_{L^1} + \|E_h^J(0, x)\|_{L^1}) \\
&\leq 2(\|U_h^I(0, x)\|_{L^1} + \|U_h^J(0, x)\|_{L^1}).
\end{aligned}$$

The proof is completed.  $\blacksquare$

#### 4.2. 2D Case

For the sake of convenience, this subsection will use the symbol  $\mathbf{x} = (x, y)$  to replace the independent variables  $(x_1, x_2)$  in (1). Let  $\{I_{i,j} = (x_{i-\frac{1}{2}}, x_{i+\frac{1}{2}}) \times (y_{j-\frac{1}{2}}, y_{j+\frac{1}{2}})\}$  be a uniform partition of the 2D spatial domain  $\Omega$  with constant spatial step-sizes  $\Delta x = x_{i+\frac{1}{2}} - x_{i-\frac{1}{2}}$  and  $\Delta y = y_{j+\frac{1}{2}} - y_{j-\frac{1}{2}}$  in the  $x$  and  $y$  directions, respectively, and  $\{J_{i+\frac{1}{2},j+\frac{1}{2}} = (x_i, x_{i+1}) \times (y_j, y_{j+1})\}$  be the dual partition. The 2D central DG methods seek two approximate solutions  $U_h^I$  and  $U_h^J$  respectively defined on those mutually dual meshes  $\{I_{i,j}\}$  and  $\{J_{i+\frac{1}{2},j+\frac{1}{2}}\}$ , where for each time  $t \in (0, T_f]$ , each component of  $U_h^I$  (resp.  $U_h^J$ ) belongs to the finite dimensional space of discontinuous piecewise polynomial functions,  $\mathcal{V}_h^I$  (resp.  $\mathcal{V}_h^J$ ), defined by

$$\begin{aligned}
\mathcal{V}_h^I &:= \{w(\mathbf{x}) \in L^1(\Omega) \mid w(\mathbf{x})|_{I_{i,j}} \in \mathbb{P}^K(I_{i,j})\}, \\
\mathcal{V}_h^J &:= \left\{ w(\mathbf{x}) \in L^1(\Omega) \mid w(\mathbf{x})|_{J_{i+\frac{1}{2},j+\frac{1}{2}}} \in \mathbb{P}^K(J_{i+\frac{1}{2},j+\frac{1}{2}}) \right\},
\end{aligned}$$

where  $\mathbb{P}^K(I_{i,j})$  and  $\mathbb{P}^K(J_{i+\frac{1}{2},j+\frac{1}{2}})$  denote two spaces of polynomial of degree at most  $K$  on the cells  $I_{i,j}$  and  $J_{i+\frac{1}{2},j+\frac{1}{2}}$ , respectively, and their dimension is equal to  $K_d := (K+1)(K+2)/2$ .

If letting  $\{\Phi_{i,j}^{(\mu)}(\mathbf{x})\}_{\mu=0}^{K_d-1}$  and  $\left\{ \Phi_{i+\frac{1}{2},j+\frac{1}{2}}^{(\mu)}(\mathbf{x}) \right\}_{\mu=0}^{K_d-1}$  denote the local orthogonal bases of the spaces  $\mathbb{P}^K(I_{i,j})$  and  $\mathbb{P}^K(J_{i+\frac{1}{2},j+\frac{1}{2}})$ , respectively, then the central DG approximate solutions  $U_h^I$  and  $U_h^J$  may be expressed as

$$U_h^I(t, \mathbf{x}) = \sum_{\mu=0}^{K_d-1} U_{i,j}^{I,(\mu)}(t) \Phi_{i,j}^{(\mu)}(\mathbf{x}) =: U_{i,j}^I(t, \mathbf{x}), \quad \mathbf{x} \in I_{i,j}, \tag{45}$$

and

$$\begin{aligned} U_h^J(t, \mathbf{x}) &= \sum_{\mu=0}^{K_d-1} U_{i+\frac{1}{2}j+\frac{1}{2}}^{J,(\mu)}(t) \Phi_{i+\frac{1}{2}j+\frac{1}{2}}^{(\mu)}(\mathbf{x}) \\ &=: U_{i+\frac{1}{2}j+\frac{1}{2}}^J(t, \mathbf{x}), \quad \mathbf{x} \in J_{i+\frac{1}{2}j+\frac{1}{2}}. \end{aligned} \quad (46)$$

Similar to the 1D case, the semi-discrete 2D central DG methods for  $U_h^I$  and  $U_h^J$  may be respectively given by

$$\begin{aligned} &\sum_{\mu=0}^{K_d-1} \left( \iint_{I_{i,j}} \Phi_{i,j}^{(\mu)}(\mathbf{x}) \Phi_{i,j}^{(\nu)}(\mathbf{x}) d\mathbf{x} \right) \frac{dU_{i,j}^{J,(\mu)}(t)}{dt} \\ &= \frac{1}{\tau_{\max}} \iint_{I_{i,j}} (U_h^J - U_h^I) \Phi_{i,j}^{(\nu)}(\mathbf{x}) d\mathbf{x} \\ &\quad + \frac{\Delta x \Delta y}{4} \sum_{\alpha=1}^Q \sum_{\beta=1}^Q \sum_{m \in \{-1,1\}} \\ &\quad \omega_\alpha \omega_\beta \left( \mathbf{F} \left( U_h^J(t, x_{i+\frac{\ell}{4}}^\alpha, y_{j+\frac{m}{4}}^\beta) \right) \right. \\ &\quad \cdot \nabla \Phi_{i,j}^{(\nu)}(x_{i+\frac{\ell}{4}}^\alpha, y_{j+\frac{m}{4}}^\beta) \Big) \\ &\quad - \frac{\Delta y}{2} \sum_{\beta=1}^Q \sum_{m,s \in \{-1,1\}} s \omega_\beta \mathbf{F}_1 \left( U_h^J(t, x_{i+\frac{s}{2}}, y_{j+\frac{m}{4}}^\beta) \right) \\ &\quad \times \Phi_{i,j}^{(\nu)}(x_{i+\frac{s}{2}}, y_{j+\frac{m}{4}}^\beta) \\ &\quad - \frac{\Delta x}{2} \sum_{\alpha=1}^Q \sum_{\ell,s \in \{-1,1\}} s \omega_\alpha \mathbf{F}_2 \left( U_h^J(t, x_{i+\frac{\ell}{4}}^\alpha, y_{j+\frac{s}{2}}) \right) \\ &\quad \times \Phi_{i,j}^{(\nu)}(x_{i+\frac{\ell}{4}}^\alpha, y_{j+\frac{s}{2}}), \end{aligned} \quad (47)$$

and

$$\begin{aligned} &\sum_{\mu=0}^{K_d-1} \left( \iint_{J_{i+\frac{1}{2}j+\frac{1}{2}}} \Phi_{i+\frac{1}{2}j+\frac{1}{2}}^{(\mu)}(\mathbf{x}) \Phi_{i+\frac{1}{2}j+\frac{1}{2}}^{(\nu)}(\mathbf{x}) d\mathbf{x} \right) \\ &\quad \times \frac{dU_{i+\frac{1}{2}j+\frac{1}{2}}^{J,(\mu)}(t)}{dt} = \frac{1}{\tau_{\max}} \iint_{J_{i+\frac{1}{2}j+\frac{1}{2}}} (U_h^I - U_h^J) \Phi_{i+\frac{1}{2}j+\frac{1}{2}}^{(\nu)}(\mathbf{x}) d\mathbf{x} \\ &\quad + \frac{\Delta x \Delta y}{4} \sum_{\alpha=1}^Q \sum_{\beta=1}^Q \sum_{m \in \{-1,1\}} \\ &\quad \times \omega_\alpha \omega_\beta \left( \mathbf{F} \left( U_h^I(t, x_{i+\frac{\ell+2}{4}}^\alpha, y_{j+\frac{m+2}{4}}^\beta) \right) \right. \\ &\quad \cdot \nabla \Phi_{i,j}^{(\nu)}(x_{i+\frac{\ell+2}{4}}^\alpha, y_{j+\frac{m+2}{4}}^\beta) \Big) \\ &\quad - \frac{\Delta y}{2} \sum_{\beta=1}^Q \sum_{m,s \in \{-1,1\}} s \omega_\beta \mathbf{F}_1 \left( U_h^I(t, x_{i+\frac{s+1}{2}}, y_{j+\frac{m+2}{4}}^\beta) \right) \\ &\quad \times \Phi_{i+\frac{1}{2}j+\frac{1}{2}}^{(\nu)}(x_{i+\frac{s+1}{2}}, y_{j+\frac{m+2}{4}}^\beta) \\ &\quad - \frac{\Delta x}{2} \sum_{\alpha=1}^Q \sum_{\ell,s \in \{-1,1\}} s \omega_\alpha \mathbf{F}_2 \left( U_h^I(t, x_{i+\frac{\ell+2}{4}}^\alpha, y_{j+\frac{s+1}{2}}) \right) \\ &\quad \times \Phi_{i+\frac{1}{2}j+\frac{1}{2}}^{(\nu)}(x_{i+\frac{\ell+2}{4}}^\alpha, y_{j+\frac{s+1}{2}}), \end{aligned} \quad (48)$$

where  $\nu = 0, \dots, K_d - 1$ ,  $\mathbf{F} = (\mathbf{F}_1, \mathbf{F}_2)$ ,  $\left\{ x_{i\pm\frac{1}{4}}^\alpha \right\}_{\alpha=1}^Q$  and  $\left\{ y_{j\pm\frac{1}{4}}^\alpha \right\}_{\alpha=1}^Q$  denote the Gaussian nodes transformed into the interval  $\left[ x_{i\pm\frac{1}{4}} - \frac{\Delta x}{4}, x_{i\pm\frac{1}{4}} + \frac{\Delta x}{4} \right]$  and  $\left[ y_{j\pm\frac{1}{4}} - \frac{\Delta y}{4}, y_{j\pm\frac{1}{4}} + \frac{\Delta y}{4} \right]$ , respectively, and the associated Gaussian quadrature weights  $\{\omega_\alpha\}_{\alpha=1}^Q$  satisfy  $\omega_\alpha > 0$  and  $\sum_{\alpha=1}^Q \omega_\alpha = 1$ . For the accuracy requirement,  $Q$  should be not less than  $K + 1$  for a  $\mathbb{P}^K$ -based central DG method (Cockburn et al. 1990).

If taking the bases as the scaled Legendre polynomials such that  $\Phi_{i,j}^{(0)}(\mathbf{x}) = \Phi_{i+\frac{1}{2}j+\frac{1}{2}}^{(0)}(\mathbf{x}) = 1$ , then from (47)–(48) with  $\nu = 0$ , one may derive the evolution equations for the cell-averages of  $U_h^I$  and  $U_h^J$  as follows

$$\begin{aligned} \frac{dU_{i,j}^{I,(0)}(t)}{dt} &= \frac{1}{\tau_{\max}} \frac{1}{\Delta x \Delta y} \iint_{I_{i,j}} (U_h^J - U_h^I) d\mathbf{x} dy \\ &\quad - \frac{1}{2} \sum_{\beta=1}^Q \sum_{lm,s \in \{-1,1\}} s \omega_\beta \left( \frac{1}{\Delta x} \mathbf{F}_1 \left( U_h^J(t, x_{i+\frac{s}{2}}, y_{j+\frac{m}{4}}^\beta) \right) \right. \\ &\quad \left. + \frac{1}{\Delta y} \mathbf{F}_2 \left( U_h^J(t, x_{i+\frac{\ell}{4}}^\beta, y_{j+\frac{s}{2}}) \right) \right) \\ &=: \mathcal{L}_{i,j}^I(U_h^I, U_h^J), \end{aligned} \quad (49)$$

and

$$\begin{aligned} \frac{dU_{i+\frac{1}{2}j+\frac{1}{2}}^{J,(0)}(t)}{dt} &= \frac{1}{\tau_{\max}} \frac{1}{\Delta x \Delta y} \iint_{J_{i+\frac{1}{2}j+\frac{1}{2}}} (U_h^I - U_h^J) d\mathbf{x} dy \\ &\quad - \frac{1}{2} \sum_{\beta=1}^Q \sum_{lm,s \in \{-1,1\}} s \omega_\beta \left( \frac{1}{\Delta x} \mathbf{F}_1 \left( U_h^I(t, x_{i+\frac{s+1}{2}}, y_{j+\frac{m+2}{4}}^\beta) \right) \right. \\ &\quad \left. + \frac{1}{\Delta y} \mathbf{F}_2 \left( U_h^I(t, x_{i+\frac{\ell+2}{4}}^\beta, y_{j+\frac{s+1}{2}}) \right) \right) \\ &=: \mathcal{L}_{i+\frac{1}{2}j+\frac{1}{2}}^J(U_h^I, U_h^J), \end{aligned} \quad (50)$$

If the time derivatives in (47)–(48) are approximated by using the SSP Runge–Kutta or multi-step methods, e.g., (36) or (37), then the fully discrete 2D central DG methods may be obtained. In the following, the PCP technique is discussed for the above 2D central DG methods. First, it may be proved that the 2D central DG methods with  $K = 0$  are PCP under a CFL-type condition.

**Theorem 4.5.** *If  $K = 0$  and  $U_{i,j}^I, U_{i+\frac{1}{2}j+\frac{1}{2}}^J \in \mathcal{G}$  for all  $i$  and  $j$ , then under the CFL type condition*

$$0 < \frac{\Delta t}{\Delta x} + \frac{\Delta t}{\Delta y} < \frac{\theta}{2c}, \quad \theta \in (0, 1], \quad (51)$$

one has

$$\begin{aligned} U_{i,j}^I + \Delta t \mathcal{L}_{i,j}^I(U_h^I, U_h^J) &\in \mathcal{G}, \\ U_{i+\frac{1}{2}j+\frac{1}{2}}^J + \Delta t \mathcal{L}_{i+\frac{1}{2}j+\frac{1}{2}}^J(U_h^I, U_h^J) &\in \mathcal{G}, \end{aligned}$$

for all  $i$  and  $j$ .

**Proof.** Because both  $U_{i,j}^I$  and  $U_{i+\frac{1}{2},j+\frac{1}{2}}^J$  are constant when  $K = 0$ , one has

$$\begin{aligned}
& U_{i,j}^I + \Delta t \mathcal{L}_{i,j}^I(U_h^I, U_h^I) \\
&= U_{i,j}^I + \frac{\theta}{\Delta x \Delta y} \iint_{I_{i,j}} (U_h^J - U_{i,j}^I) dx dy \\
&\quad - \frac{1}{2} \sum_{m,s \in \{-1,1\}} s \left( \frac{\Delta t}{\Delta x} F_1 \left( U_{i+\frac{s}{2},j+\frac{m}{2}}^J \right) \right. \\
&\quad \left. + \frac{\Delta t}{\Delta y} F_2 \left( U_{i+\frac{s}{2},j+\frac{m}{2}}^J \right) \right) \\
&= (1 - \theta) U_{i,j}^I + \frac{\theta}{4} \sum_{m,s \in \{-1,1\}} U_{i+\frac{s}{2},j+\frac{m}{2}}^J \\
&\quad - \frac{1}{2} \sum_{m,s \in \{-1,1\}} \left( \frac{\Delta t}{\Delta x} s F_1 \left( U_{i+\frac{s}{2},j+\frac{m}{2}}^J \right) \right. \\
&\quad \left. + \frac{\Delta t}{\Delta y} m F_2 \left( U_{i+\frac{s}{2},j+\frac{m}{2}}^J \right) \right) \\
&= (1 - \theta) U_{i,j}^I + \frac{\theta}{4} \sum_{m,s \in \{-1,1\}} \left( \frac{\Delta y}{\Delta x + \Delta y} U_{i+\frac{s}{2},j+\frac{m}{2}}^{J,[1]} \right. \\
&\quad \left. + \frac{\Delta x}{\Delta x + \Delta y} U_{i+\frac{s}{2},j+\frac{m}{2}}^{J,[2]} \right), \tag{52}
\end{aligned}$$

where

$$\begin{aligned}
U_{i+\frac{s}{2},j+\frac{m}{2}}^{J,[1]} &:= U_{i+\frac{s}{2},j+\frac{m}{2}}^J \\
&\quad - \frac{2s}{\theta} \left( \frac{\Delta t}{\Delta x} + \frac{\Delta t}{\Delta y} \right) F_1 \left( U_{i+\frac{s}{2},j+\frac{m}{2}}^J \right), \\
U_{i+\frac{s}{2},j+\frac{m}{2}}^{J,[2]} &:= U_{i+\frac{s}{2},j+\frac{m}{2}}^J \\
&\quad - \frac{2m}{\theta} \left( \frac{\Delta t}{\Delta x} + \frac{\Delta t}{\Delta y} \right) F_2 \left( U_{i+\frac{s}{2},j+\frac{m}{2}}^J \right).
\end{aligned}$$

Thanks to the Lax–Friedrichs splitting property in Lemma 3.4,  $U_{i+\frac{s}{2},j+\frac{m}{2}}^{J,[1]}, U_{i+\frac{s}{2},j+\frac{m}{2}}^{J,[2]} \in \mathcal{G}$  under the theorem hypothesis. Combining those with (52) and using the convexity of  $\mathcal{G}$  further yields  $U_{i,j}^I + \Delta t \mathcal{L}_{i,j}^I(U_h^I, U_h^I) \in \mathcal{G}$ . Similar arguments may yield  $U_{i+\frac{1}{2},j+\frac{1}{2}}^J + \Delta t \mathcal{L}_{i+\frac{1}{2},j+\frac{1}{2}}^J(U_h^J, U_h^J) \in \mathcal{G}$ . The proof is completed.

Theorem 4.5 indicates that the first-order accurate 2D central DG method is PCP under the CFL type condition (51) if the forward Euler method is used for time discretization. Similar to the 1D case, it is important to find out a sufficient condition on the polynomial vectors  $U_{i,j}^I(\mathbf{x})$  and  $U_{i+\frac{1}{2},j+\frac{1}{2}}^J(\mathbf{x})$  in a high-order accurate PCP central DG method. For the sake of convenience, omit the independent variable  $t$  temporarily, and let  $\{\hat{x}_{i\pm\frac{1}{4}}^\alpha\}_{\alpha=1}^L$  and  $\{\hat{y}_{j\pm\frac{1}{4}}^\alpha\}_{\alpha=1}^L$  be the Gauss–Lobatto nodes transformed into the interval  $[x_{i\pm\frac{1}{4}} - \frac{\Delta x}{4}, x_{i\pm\frac{1}{4}} + \frac{\Delta x}{4}]$  and  $[y_{j\pm\frac{1}{4}} - \frac{\Delta y}{4}, y_{j\pm\frac{1}{4}} + \frac{\Delta y}{4}]$ , respectively, and  $\{\hat{\omega}_\alpha\}_{\alpha=1}^L$  be the associated Gaussian quadrature weights satisfying  $\hat{\omega} > 0$  and  $\sum_{\alpha=1}^L \hat{\omega}_\alpha = 1$ , where  $L \geq (K+3)/2$ .

**Theorem 4.6.** If  $U_{i,j}^I(\hat{x}_{i+\frac{s}{4}}^\alpha, y_{j+\frac{m}{4}}^\beta) \in \mathcal{G}$  and  $U_{i+\frac{1}{2},j+\frac{1}{2}}^J(x_{i+\frac{1}{2}+\frac{s}{4}}^\beta, \hat{y}_{j+\frac{1}{2}+\frac{m}{4}}^\alpha) \in \mathcal{G}$  for all  $i, j \in \mathbb{Z}$ ,  $s, m \in \{-1, 1\}$ ,  $\alpha = 1, 2, \dots, L$ , and  $\beta = 1, 2, \dots, Q$ , then under the CFL type condition

$$0 < \frac{\Delta t}{\Delta x} + \frac{\Delta t}{\Delta y} \leq \frac{\hat{\omega}_1 \theta}{2c}, \quad \theta \in (0, 1], \tag{53}$$

one has

$$\begin{aligned}
& U_{i,j}^{I,(0)} + \Delta t \mathcal{L}_{i,j}^I(U_h^I, U_h^J) \in \mathcal{G}, \\
& U_{i+\frac{1}{2},j+\frac{1}{2}}^{J,(0)} + \Delta t \mathcal{L}_{i+\frac{1}{2},j+\frac{1}{2}}^J(U_h^J, U_h^I) \in \mathcal{G},
\end{aligned}$$

for all  $i$  and  $j$ .

**Proof.** Using the convexity of  $\mathcal{G}$  and the exactness of the Gauss–Lobatto quadrature rule with  $L$  nodes, and the Gauss quadrature rule with  $Q$  nodes for the polynomials of degree  $K$ , yields

$$\begin{aligned}
& \frac{1}{\Delta x \Delta y} \iint_{I_{i,j}} U_h^J dx dy \\
&= \frac{1}{\Delta x} \int_{x_{i-\frac{1}{2}}}^{x_{i+\frac{1}{2}}} \left( \frac{1}{2} \sum_{\beta=1m \in \{-1,1\}} \omega_\beta U_h^J(x, y_{j+\frac{m}{4}}^\beta) \right) dx \\
&= \frac{1}{2} \sum_{\beta=1m \in \{-1,1\}} \omega_\beta \left( \frac{1}{\Delta x} \int_{x_{i-\frac{1}{2}}}^{x_{i+\frac{1}{2}}} U_h^J(x, y_{j+\frac{m}{4}}^\beta) dx \right) \\
&= \frac{1}{2} \sum_{\beta=1m \in \{-1,1\}} \omega_\beta \left( \frac{1}{2} \sum_{\alpha=1s \in \{-1,1\}}^L \hat{\omega}_\alpha U_h^J(\hat{x}_{i+\frac{s}{4}}^\alpha, y_{j+\frac{m}{4}}^\beta) \right) \\
&= \frac{1}{2} \sum_{\beta=1m \in \{-1,1\}} \omega_\beta \left( \frac{\hat{\omega}_1}{2} \sum_{s \in \{-1,1\}} U_h^J(x_{i+\frac{s}{2}}, y_{j+\frac{m}{4}}^\beta) \right. \\
&\quad \left. + (1 - \hat{\omega}_1) \Xi_{i,j+\frac{m}{4}}^\beta \right), \tag{54}
\end{aligned}$$

where

$$\begin{aligned}
\Xi_{i,j+\frac{m}{4}}^\beta &:= \frac{1}{2(1 - \hat{\omega}_1)} \left( \sum_{\alpha=2}^L \hat{\omega}_\alpha U_h^J(\hat{x}_{i-\frac{1}{4}}^\alpha, y_{j+\frac{m}{4}}^\beta) \right. \\
&\quad \left. + \sum_{\alpha=1}^{L-1} \hat{\omega}_\alpha U_h^J(\hat{x}_{i+\frac{1}{4}}^\alpha, y_{j+\frac{m}{4}}^\beta) \right) \in \mathcal{G},
\end{aligned}$$

and  $\hat{\omega}_1 = \hat{\omega}_L \leq \frac{1}{2}$  has been used. Similarly, one has

$$\begin{aligned}
& \frac{1}{\Delta x \Delta y} \iint_{I_{i,j}} U_h^I dx dy = \frac{1}{2} \sum_{\beta=1m \in \{-1,1\}} \omega_\beta \\
&\quad \times \left( \frac{\hat{\omega}_1}{2} \sum_{s \in \{-1,1\}} U_h^I(x_{i+\frac{s}{2}}, y_{j+\frac{s}{2}}^\beta) + (1 - \hat{\omega}_1) \Xi_{i+\frac{m}{4},j}^\beta \right), \tag{55}
\end{aligned}$$

with

$$\Xi_{i+\frac{m}{4}j}^\beta := \frac{1}{2(1-\hat{\omega}_1)} \left( \sum_{\alpha=2}^L \hat{\omega}_\alpha \mathbf{U}_h^J(x_{i+\frac{m}{4}}^\beta, \hat{y}_{j-\frac{1}{4}}^\alpha) + \sum_{\alpha=1}^{L-1} \hat{\omega}_\alpha \mathbf{U}_h^J(x_{i+\frac{m}{4}}^\beta, \hat{y}_{j+\frac{1}{4}}^\alpha) \right) \in \mathcal{G},$$

and

$$\mathbf{U}_{i,j}^{I,(0)} = \frac{1}{2} \sum_{\beta=1}^Q \sum_{lm \in \{-1,1\}} \omega_\beta \left( \frac{1}{2} \sum_{\alpha=1}^L \sum_{ls \in \{-1,1\}} \hat{\omega}_\alpha \mathbf{U}_h^I(\hat{x}_{i+\frac{s}{4}}^\alpha, y_{j+\frac{m}{4}}^\beta) \right) \in \mathcal{G}.$$

Combining (54) and (55) gives

$$\begin{aligned} \frac{1}{\Delta x \Delta y} \iint_{I_{i,j}} \mathbf{U}_h^J dx dy &= \frac{\lambda_x}{\lambda_x + \lambda_y} \frac{1}{\Delta x \Delta y} \iint_{I_{i,j}} \mathbf{U}_h^J dx dy \\ &\quad + \frac{\lambda_y}{\lambda_x + \lambda_y} \frac{1}{\Delta x \Delta y} \iint_{I_{i,j}} \mathbf{U}_h^J dx dy \\ &= \frac{1}{2} \sum_{\beta=1}^Q \sum_{lm \in \{-1,1\}} \omega_\beta \left( \frac{\hat{\omega}_1}{2(\lambda_x + \lambda_y)} \right. \\ &\quad \times \sum_{s \in \{-1,1\}} \left( \lambda_x \mathbf{U}_h^J(x_{i+\frac{s}{4}}^\beta, y_{j+\frac{m}{4}}^\beta) \right. \\ &\quad \left. \left. + \lambda_y \mathbf{U}_h^J(x_{i+\frac{m}{4}}^\beta, y_{j+\frac{s}{2}}^\beta) \right) \right) \\ &\quad + \frac{1}{2} \sum_{\beta=1}^Q \sum_{lm \in \{-1,1\}} \omega_\beta (1 - \hat{\omega}_1) \Xi_{i,j}^{\beta,m}, \end{aligned} \quad (56)$$

where  $\lambda_x := \Delta t / \Delta x$ ,  $\lambda_y := \Delta t / \Delta y$ , and

$$\Xi_{i,j}^{\beta,m} := \frac{\lambda_x}{\lambda_x + \lambda_y} \Xi_{i,j+\frac{m}{4}}^\beta + \frac{\lambda_y}{\lambda_x + \lambda_y} \Xi_{i+\frac{m}{4}j}^\beta \in \mathcal{G}.$$

Therefore, one gets

$$\begin{aligned} \mathbf{U}_{i,j}^{I,(0)} + \Delta t \mathcal{L}_{i,j}^I(\mathbf{U}_h^I, \mathbf{U}_h^J) &= (1 - \theta) \mathbf{U}_{i,j}^{I,(0)} \\ &\quad + \frac{\theta}{\Delta x \Delta y} \iint_{I_{i,j}} \mathbf{U}_h^J dx dy \\ &\quad - \frac{1}{2} \sum_{\beta=1}^Q \sum_{s \in \{-1,1\}} s \omega_\beta \left( \lambda_x \mathbf{F}_1 \left( \mathbf{U}_h^J(x_{i+\frac{s}{4}}^\beta, y_{j+\frac{m}{4}}^\beta) \right) \right. \\ &\quad \left. + \lambda_y \mathbf{F}_2 \left( \mathbf{U}_h^J(x_{i+\frac{m}{4}}^\beta, y_{j+\frac{s}{2}}^\beta) \right) \right) \\ &\stackrel{(56)}{=} (1 - \theta) \mathbf{U}_{i,j}^{I,(0)} + \frac{\theta}{2} \sum_{\beta=1}^Q \sum_{lm \in \{-1,1\}} \omega_\beta (1 - \hat{\omega}_1) \Xi_{i,j}^{\beta,m} \\ &\quad + \frac{\theta}{2} \sum_{\beta=1}^Q \sum_{s \in \{-1,1\}} \frac{\omega_\beta \hat{\omega}_1}{2} \left( \frac{\lambda_x}{\lambda_x + \lambda_y} \mathbf{U}_{i+\frac{s}{4}j+\frac{m}{4}}^{J,\beta} \right. \\ &\quad \left. + \frac{\lambda_y}{\lambda_x + \lambda_y} \mathbf{U}_{i+\frac{m}{4}j+\frac{s}{2}}^{J,\beta} \right), \end{aligned} \quad (57)$$

where

$$\begin{aligned} \mathbf{U}_{i+\frac{s}{4}j+\frac{m}{4}}^{J,\beta} &:= \mathbf{U}_h^J(x_{i+\frac{s}{4}}^\beta, y_{j+\frac{m}{4}}^\beta) \\ &\quad - \frac{2s(\lambda_x + \lambda_y)}{\theta \hat{\omega}_1} \mathbf{F}_1 \left( \mathbf{U}_h^J(x_{i+\frac{s}{4}}^\beta, y_{j+\frac{m}{4}}^\beta) \right) \in \mathcal{G} \cup \partial \mathcal{G}, \\ \mathbf{U}_{i+\frac{m}{4}j+\frac{s}{2}}^{J,\beta} &:= \mathbf{U}_h^J(x_{i+\frac{m}{4}}^\beta, y_{j+\frac{s}{2}}^\beta) \\ &\quad - \frac{2s(\lambda_x + \lambda_y)}{\theta \hat{\omega}_1} \mathbf{F}_2 \left( \mathbf{U}_h^J(x_{i+\frac{m}{4}}^\beta, y_{j+\frac{s}{2}}^\beta) \right) \in \mathcal{G} \cup \partial \mathcal{G}, \end{aligned}$$

due to the Lax–Friedrichs splitting property in Lemma 3.4 and the theorem hypothesis. Using (57) and the convexity of  $\mathcal{G}$  further yields  $\mathbf{U}_{i,j}^{I,(0)} + \Delta t \mathcal{L}_{i,j}^I(\mathbf{U}_h^I, \mathbf{U}_h^J) \in \mathcal{G}$ . Similar arguments yield  $\mathbf{U}_{i+\frac{1}{2}j+\frac{1}{2}}^{J,(0)} + \Delta t \mathcal{L}_{i+\frac{1}{2}j+\frac{1}{2}}^J(\mathbf{U}_h^J, \mathbf{U}_h^I) \in \mathcal{G}$ . The proof is completed.  $\blacksquare$

Although the sufficient condition for the 2D high-order accurate central DG methods in Theorem 4.6 is given only for the forward Euler time discretization, it is also valid for the high-order accurate SSP time discretization (36) or (37), which has been expressed as a convex combination of the forward Euler method. Built on the above theoretical results, the 2D PCP limiting procedure may be presented and is very similar to the 1D case so that its details may be omitted here. The only difference is that the 2D PCP limiter is used to ensure the admissibility of  $\mathbf{U}_h^I(\mathbf{x})$  and  $\mathbf{U}_h^J(\mathbf{x})$  at the following points

$$\mathcal{S}_{ij} = (\hat{\mathcal{S}}_i^x \otimes \mathcal{S}_j^y) \cup (\mathcal{S}_i^x \otimes \hat{\mathcal{S}}_j^y) \cup (\mathcal{S}_i^x \otimes \mathcal{S}_j^y),$$

for all  $i$  and  $j$ , where  $\otimes$  denotes the tensor product of sets, and

$$\begin{aligned} \hat{\mathcal{S}}_i^x &:= \left\{ \hat{x}_{i-\frac{1}{4}}^\alpha \right\}_{\alpha=1}^L \cup \left\{ \hat{x}_{i+\frac{1}{4}}^\alpha \right\}_{\alpha=1}^L, \\ \mathcal{S}_i^x &:= \left\{ x_{i-\frac{1}{4}}^\beta \right\}_{\beta=1}^Q \cup \left\{ x_{i+\frac{1}{4}}^\beta \right\}_{\beta=1}^Q, \\ \hat{\mathcal{S}}_j^y &:= \left\{ \hat{y}_{j-\frac{1}{4}}^\alpha \right\}_{\alpha=1}^L \cup \left\{ \hat{y}_{j+\frac{1}{4}}^\alpha \right\}_{\alpha=1}^L, \\ \mathcal{S}_j^y &:= \left\{ y_{j-\frac{1}{4}}^\beta \right\}_{\beta=1}^Q \cup \left\{ y_{j+\frac{1}{4}}^\beta \right\}_{\beta=1}^Q. \end{aligned}$$

If replacing the solution polynomials of high-order accurate central DG methods with the limited polynomials at each stage of SSP Runge–Kutta method (36) or each step of SSP multi-step method (37), then using Theorem 4.2 may prove that the resulting 2D fully discrete central DG methods are PCP under some CFL type conditions.

**Theorem 4.7.** *If the 2D high-order accurate central DG solution polynomials are revised to the above limited polynomials at each stage of SSP Runge–Kutta method (36) or each step of multi-step method (37), then (i) the resulting Runge–Kutta central DG methods are PCP under the CFL type condition (53), (ii) the resulting multi-step central DG scheme is PCP under the CFL type condition*

$$0 < \frac{\Delta t}{\Delta x} + \frac{\Delta t}{\Delta y} \leq \frac{\hat{\omega}_1 \theta}{2c}, \quad \theta \in \left(0, \frac{1}{3}\right]. \quad (58)$$

It is worth mentioning that the resulting 2D PCP central DG methods are also  $L^1$ -stable, similar to Theorem 4.4.



**Table 1**  
Example 5.1: numerical  $l^1$ - and  $l^2$ -errors and Orders at  $t = 0.2$  of PCPRKCDGP2 and PCPMSCDGP2 for the Ideal EOS with  $\Gamma = 5/3$

$N$	PCPRKCDGP2				PCPMSCDGP2			
	$l^1$ error	$l^1$ order	$l^2$ error	$l^2$ order	$l^1$ error	$l^1$ order	$l^2$ error	$l^2$ order
10	2.402e-4	...	3.102e-4	...	1.987e-4	...	2.430e-4	...
20	3.439e-5	2.80	4.988e-5	2.64	2.290e-5	3.12	2.948e-5	3.04
40	5.031e-6	2.77	9.328e-6	2.42	2.845e-6	3.01	3.686e-6	3.00
80	6.036e-7	3.06	1.180e-6	2.98	3.564e-7	3.00	4.611e-7	3.00
160	4.458e-8	3.76	5.767e-8	4.35	4.456e-8	3.00	5.766e-8	3.00
320	5.573e-9	3.00	7.209e-9	3.00	5.570e-9	3.00	7.207e-9	3.00

## 5. NUMERICAL EXPERIMENTS

This section conducts several numerical experiments on the 1D and 2D, highly challenging, ultra-relativistic RHD problems with either large Lorentz factors, strong discontinuities, or low rest-mass density or pressure, to demonstrate the accuracy, robustness, and effectiveness of the proposed PCP central DG methods. For brevity, we will only present the numerical results obtained by the  $\mathbb{P}^2$ -based central DG methods with the third-order accurate Runge–Kutta time discretization (36) or multi-step time discretization (37). For convenience, we abbreviate them as “PCPRKCDGP2” and “PCPMSCDGP2,” respectively. Unless otherwise stated,  $\theta$  is taken as 1 for PCPRKCDGP2 and  $\frac{1}{3}$  for PCPMSCDGP2.

### 5.1. 1D Case

This section is to conduct four 1D numerical experiments. In all computations, the time stepsize  $\Delta t$  will be taken as  $0.5\hat{\omega}_1\theta\Delta x c^{-1}$  with  $\hat{\omega}_1 = \frac{1}{6}$ .

**Example 5.1 (1D smooth problem).** This is used to check the accuracy of the 1D PCP central DG methods. The initial data are taken as

$$\begin{aligned} V(0, x) &= (\rho(0, x), v(0, x), p(0, x))^T \\ &= (1 + 0.99999 \sin(2\pi x), 0.99, 10^{-2})^T, x \in [0, 1), \end{aligned}$$

and thus the exact solutions can be given by

$$\begin{aligned} V(t, x) &= (1 + 0.99999 \sin(x - 0.99t), 0.99, 10^{-2})^T, \\ x &\in [0, 1), t \geq 0, \end{aligned}$$

which describes a RHD sine wave propagating periodically and quickly in the interval  $[0, 1)$  with low density and pressure.

The ideal EOS (14) with  $\Gamma = \frac{5}{3}$  is first considered. Table 1 lists the  $l^1$  and  $l^2$ -errors at  $t = 0.2$  and corresponding orders obtained by using PCPRKCDGP2 and PCPMSCDGP2, respectively. The results show that the theoretical orders are obtained by both PCPRKCDGP2 and PCPMSCDGP2 and the PCP limiting procedure does not destroy the accuracy. The error graphs in Figure 1 display the same phenomenon for three different EOS.

To verify the capability of the proposed PCP central DG methods to resolve 1D ultra-relativistic wave configurations, a Riemann problem, a shock heating problem, and a blast wave interaction problem will be solved, and only numerical results of PCPMSCDGP2 will be presented in the following since the results of PCPRKCDGP2 are very similar to PCPMSCDGP2.

**Example 5.2 (1D Riemann problem).** The initial data of 1D RHD Riemann problem considered here are

$$V(0, x) = \begin{cases} (1, 0, 10^4)^T, & x < 0.5, \\ (1, 0, 10^{-8})^T, & x > 0.5. \end{cases} \quad (59)$$

The initial discontinuity will evolve as a strong left-moving rarefaction wave, a quickly right-moving contact discontinuity and a shock wave. The speeds of the contact discontinuity and shock wave are about 0.986956 and 0.9963757, respectively, for the ideal gas with  $\Gamma = 5/3$ , see (Wu & Tang 2015), such that they are very close to the speed of light and this test becomes very ultra-relativistic.

Figure 2 displays the numerical results at  $t = 0.45$ , obtained by using PCPMSCDGP2 (“o”) with 640 uniform cells within the domain  $[0, 1]$ , where the solid lines denote the exact solutions (Martí & Müller 1994) for the ideal EOS, and reference solutions for the EOS (16). The close-ups of rest-mass densities are displayed in Figure 3. Because it is difficult to get the exact solution for a general EOS, our reference solutions are numerically obtained by using the Lax–Friedrichs scheme over a very fine mesh of 100,000 uniform cells. It is worth emphasizing that the width of region between the contact discontinuity and shock wave at  $t = 0.45$  is about  $4 \times 10^{-3}$ , so it is not easy to resolve the contact discontinuity and shock wave with 640 uniform cells in the domain  $[0, 1]$ . From Figures 2 and 3, we see that PCPMSCDGP2 exhibits very good resolution and captures well the wave configuration in the extremely narrow region between the contact discontinuity and shock wave, in comparison with the fifth- and ninth-order accurate finite difference WENO schemes (Wu & Tang 2015); the maximal densities for PCPMSCDGP2 within the narrow region between the contact discontinuity and shock wave are about 92.98% of the analytic value for the ideal EOS (14), and 93.67% of the reference value for the EOS (16), respectively; the nonlinear addition of velocities yields a curved profile for the rarefaction fan, as opposed to a linear one in the non-relativistic case. and the wave configurations in Figure 2 for two EOS are different. If the PCP limiting procedure is not employed, then the high-order accurate central DG methods will break down quickly after few time steps due to nonphysical numerical solutions.

**Example 5.3 (Shock heating problem).** The test is to solve the shock heating problem (Blandford & McKee 1976). The computational domain  $[0, 1]$  with a reflecting boundary at  $x = 1$  is initially filled with a cold gas (the specific internal energy is nearly zero and taken as 0.0001 in the computations), which has a unit rest-mass density and the velocity  $v_0$  of

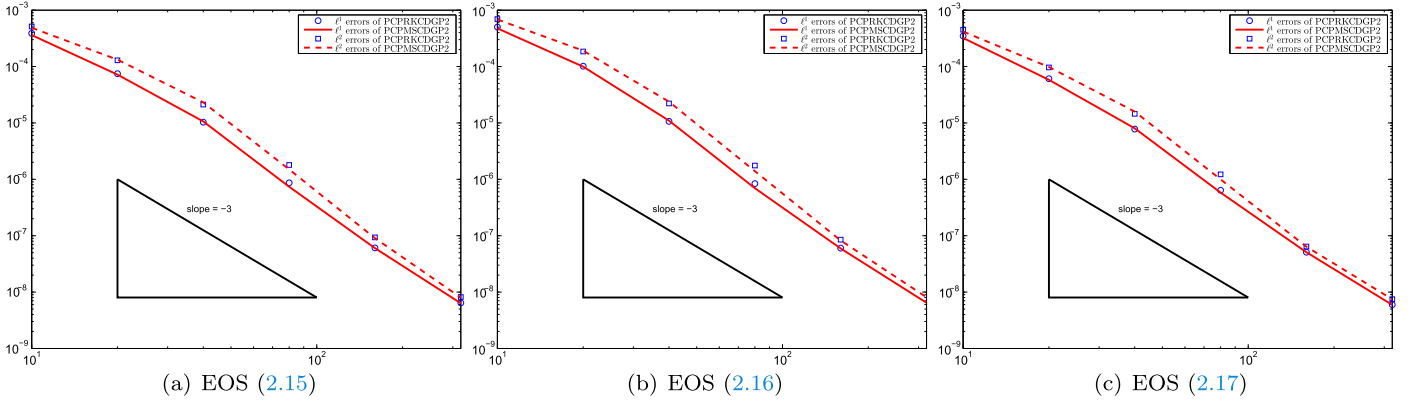


Figure 1. Example 5.1: numerical  $l^1$ - and  $l^2$ -errors at  $t = 0.2$  of PCPRKCDGP2 and PCPMSCDGP2.

$1 - 10^{-8}$ . When the initial gas moves toward to the reflecting boundary, the gas is compressed and heated as the kinetic energy is converted into the internal energy. After then, a reflected strong shock wave is formed and propagates to the left. Behind the reflected shock wave, the gas is at rest and has a specific internal energy of  $W_0 - 1$  due to the energy conservation across the shock wave,  $W_0 = (1 - v_0^2)^{-1/2}$  is about 7071.07. The compression ratio  $\sigma$  across the relativistic shock wave is about  $\sigma \approx 4W_0 + 3 \approx 28287.27$ , and grows linearly to the infinite with the Lorentz factor  $W_0$  when  $v_0$  tends to speed of light  $c$ . It is worth noting that the compression ratio across the non-relativistic shock wave is always bounded; e.g., by  $(\Gamma + 1)/(\Gamma - 1)$  for the ideal gas.

Here, we will consider the ideal EOS with the adiabatic index  $\Gamma$  of  $4/3$  and the EOS (17). Figure 4 displays the numerical solutions at  $t = 2$ , obtained by using PCPMSCDGP2 (“o”) with 200 uniform cells. It is seen that PCPMSCDGP2 exhibits good robustness for this ultra-relativistic problem and high resolution for the strong shock wave, even though there exists the well-known wall-heating phenomenon near the reflecting boundary  $x = 1$ . The difference between two different EOS is very small because of the very low specific internal energy. In this test, it is also necessary for the successful performance of the high-order accurate central DG methods to use the PCP limiting procedure.

**Example 5.4 (Blast wave interaction).** It is an initial-boundary-value problem for the RHD Equation (1) with  $d = 1$ , and very severe due to the strong relativistic shock waves and interaction between blast waves in a narrow region (Martí & Müller 1996; Yang et al. 2011; Wu & Tang 2015). The initial data are taken as

$$V(0, x) = \begin{cases} (1, 0, 1000)^T, & 0 < x < 0.1, \\ (1, 0, 0.01)^T, & 0.1 < x < 0.9, \\ (1, 0, 100)^T, & 0.9 < x < 1, \end{cases} \quad (60)$$

and the outflow boundary conditions are specified at two ends of the computational domain  $[0, 1]$ .

Figure 5 gives close-up of the solutions at  $t = 0.43$  obtained by using PCPMSCDGP2 (“o”) with 4000 uniform cells within the domain  $[0, 1]$ , where the solid lines denote the exact solutions for the ideal EOS (14) with  $\Gamma = 1.4$ , (see Martí & Müller 1996), and the reference solutions for the EOS (15) obtained by using the Lax–Friedrichs scheme over a very fine mesh of 400,000 uniform cells. We find that there are two

shock waves and two contact discontinuities in the solutions at  $t = 0.43$  within the interval  $[0.5, 0.53]$  because both initial discontinuities evolve and two blast waves collide with each other; the proposed central DG methods may well resolve those discontinuities and clearly capture the complex relativistic wave configuration, except for small oscillations between the left shock wave and contact discontinuity. The oscillations may be suppressed by locally using the nonlinear limiter, e.g., the WENO limiter (Qiu & Shu 2005; Zhao 2014), see Figure 6.

## 5.2. 2D Case

This section’s purpose is to conduct five 2D numerical experiments on a smooth problem, two Riemann problems, and two relativistic jet flows. Because the strong shock waves, as well as their interaction, appear in the last four problems, the WENO limiter will be implemented prior to the PCP limiting procedure with the aid of the local characteristic decomposition (Zhao 2014). Although it may suppress spurious oscillations, it can enhance the numerical stability of high-order accurate (central) DG methods. In particular, when the WENO limiter is locally used, a larger time stepsize is allowed. In all computations, the time stepsize  $\Delta t$  will be taken as  $\frac{\varpi \theta}{2c(1/\Delta x + 1/\Delta y)}$ , with  $\varpi = \hat{\omega}_1 = \frac{1}{6}$  for the first problem and  $\varpi = 1$  for other problems.

**Example 5.5 (2D smooth problem).** Similar to Example 5.1, this smooth problem is used to check the accuracy of proposed 2D PCP central DG methods. The initial data are taken as

$$V(0, x, y) = (1 + 0.99999 \sin(2\pi(x + y)), 0.99/\sqrt{2}, 0.99/\sqrt{2}, 10^{-2})^T,$$

so that the exact solutions are

$$V(t, x, y) = (1 + 0.99999 \sin(2\pi(x + y - 0.99\sqrt{2}t)), 0.99/\sqrt{2}, 0.99/\sqrt{2}, 10^{-2})^T,$$

which describe an RHD sine wave propagating periodically in the domain  $\Omega = [0, 1] \times [0, 1]$  at an angle  $45^\circ$  with the  $x$ -axis. The domain  $\Omega$  is divided into  $N \times N$  uniform cells and the periodic boundary conditions are specified on  $\partial\Omega$ .

The ideal EOS (14) with  $\Gamma = \frac{5}{3}$  is first considered. Table 2 lists the  $l^1$  and  $l^2$ -errors at  $t = 0.2$  and corresponding orders obtained by using PCPRKCDGP2 and PCPMSCDGP2, respectively. The results show that the theoretical orders are obtained by both PCPRKCDGP2 and PCPMSCDGP2 and

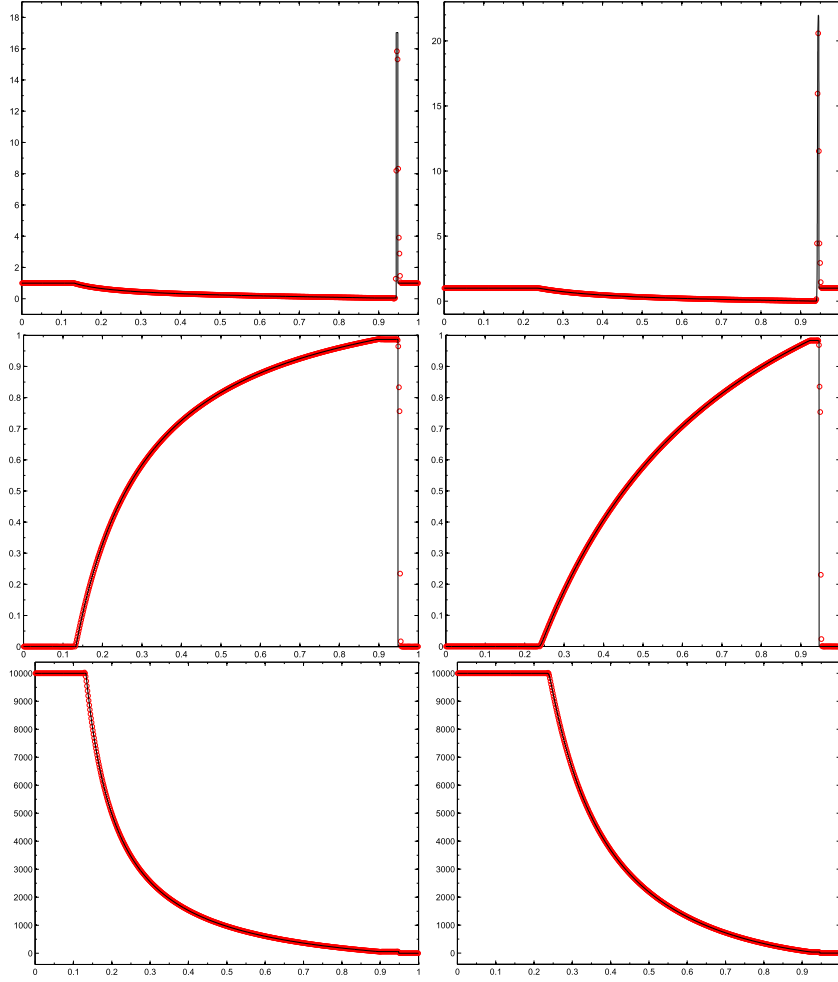


**Figure 2.** Example 5.2: The density  $\rho$ , velocity  $v_1$ , and pressure  $p$  at  $t = 0.45$  obtained by using PCPMSCDGP2 with 640 uniform cells. Left: ideal EOS (14) with  $\Gamma = 5/3$ ; right: EOS (16).

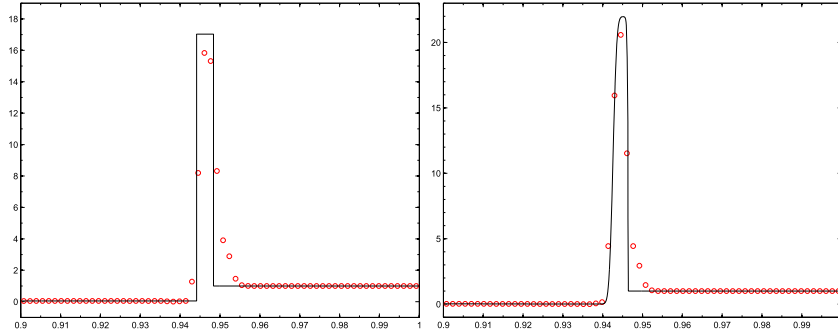


**Figure 3.** Same as Figure 2, except for the close-up of rest-mass density.

the PCP limiting procedure does not destroy the accuracy. Plots of numerical errors in Figure 7 further validate the accuracy of both PCPRKCDGP2 and PCPMSCDGP2 for the general EOS.

**Example 5.6 (2D Riemann problems).** Initial data of two Riemann problems of 2D RHD Equation (1) considered here comprise four different constant states in the unit square  $\Omega = [-1, 1] \times [-1, 1]$ , with initial discontinuities parallel to both coordinate axes, respectively. In our computations, the uniform mesh of  $400 \times 400$  cells is used, the output time is set

as 0.8, and  $\Gamma = \frac{5}{3}$  in the ideal EOS. Moreover, it is also necessary for the successful performance of the high-order accurate central DG methods to use the PCP limiting procedure.

The initial data of the first Riemann problem (Zanna & Bucciantini 2002; Lucas-Serrano et al. 2004) are

$$V(0, x, y) = \begin{cases} (0.1, 0, 0, 0.01)^T, & x > 0, y > 0, \\ (0.1, 0.99, 0, 1)^T, & x < 0, y > 0, \\ (0.5, 0, 0, 1)^T, & x < 0, y < 0, \\ (0.1, 0, 0.99, 1)^T, & x > 0, y < 0, \end{cases}$$

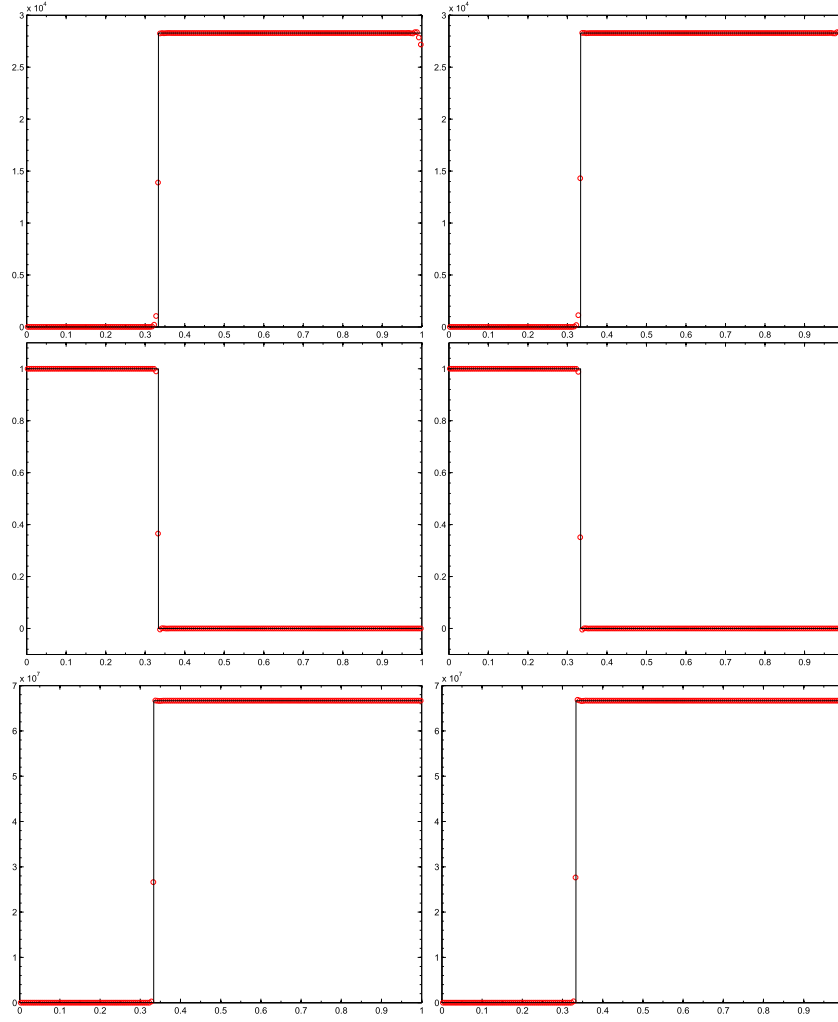


**Figure 4.** Example 5.3: The density  $\rho$ , velocity  $v_1$ , and pressure  $p$  at  $t = 2$  obtained by using PCPMSCDGP2 (“o”) with 200 uniform cells. The solid lines denote the exact solutions. Left: ideal EOS (14) with  $\Gamma = 4/3$ ; right: EOS (17).

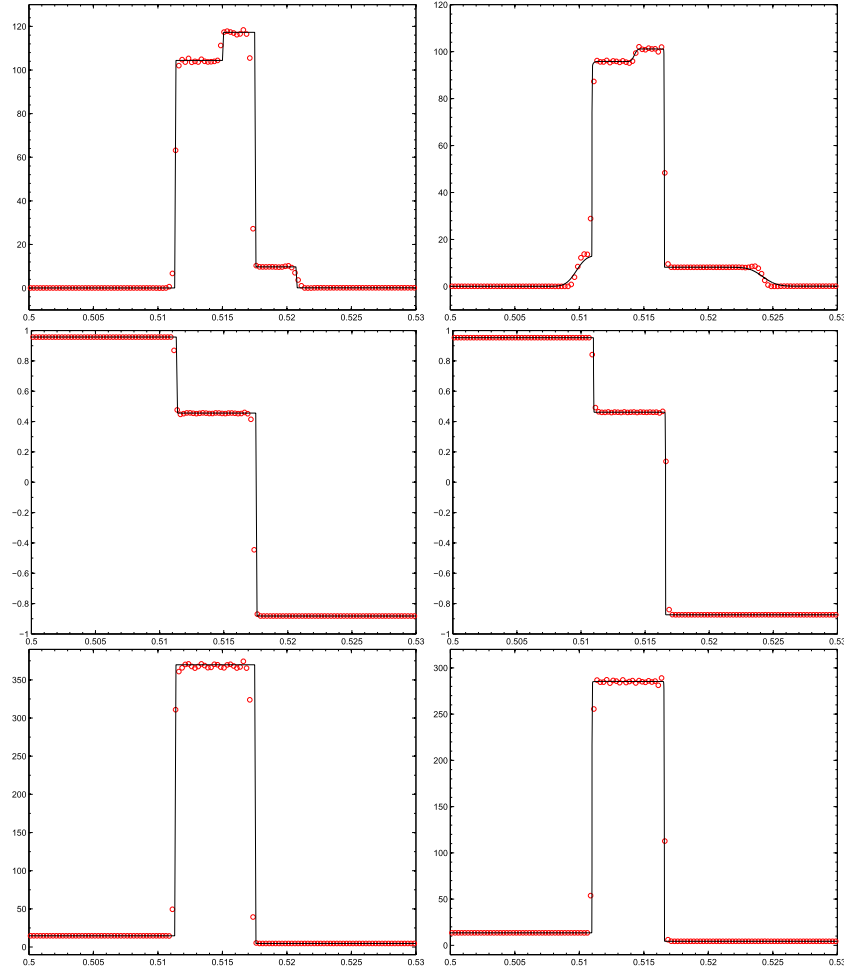
where both the left and lower discontinuities are the contact waves with a jump in the transverse velocity and rest-mass density, whereas both the right and upper are non-simple waves.

Figure 8 gives the contours of the density logarithm  $\ln \rho$  obtained by using PCPMSCDGP2 for the ideal EOS (14) and the EOS (16). The results obtained by PCPRKCDGP2 are omitted here, and hereafter, because they very similar to PCPMSCDGP2. It is found that four initial discontinuities interact each other and form two reflected curved shock waves, an elongated jet-like spike approximately between two points (0.4,0.4) and (0.8,0.8) on the line  $x = y$  when  $t = 0.8$ , and a complex mushroom structure starting from the point (0,0) and

expanding to the bottom-left region; PCPMSCDGP2 exhibits good robustness and clearly captures those complex wave configurations; the results for the ideal EOS case agrees well with those given by the high-order accurate PCP finite difference WENO in (Wu & Tang 2015); the wave configurations depend on the EOS; and the velocities of the reflected curved shock waves in the case of EOS (16) are smaller than the ideal EOS. It is worth mentioning that the high-order accurate central DG methods fail in the first time step if the PCP limiting procedure is not employed.

The initial data of the second 2D Riemann problem (Wu & Tang 2015) are

$$V(0, x, y) = \begin{cases} (0.1, 0, 0, 20)^T, & x > 0.5, y > 0.5, \\ (0.00414329639576, \\ 0.9946418833556542, 0, 0.05)^T, & x < 0.5, y > 0.5, \\ (0.01, 0, 0, 0.05)^T, & x < 0.5, y < 0.5, \\ (0.00414329639576, 0, \\ 0.9946418833556542, 0.05)^T, & x > 0.5, y < 0.5, \end{cases}$$



**Figure 5.** Example 5.4: Close-up of the numerical solutions at  $t = 0.43$ , obtained by using PCPMSCDGP2 (“o”) with 4000 uniform cells. Left: ideal EOS (14) with  $\Gamma = 1.4$ ; right: EOS (15).

in which the left and lower initial discontinuities are the contact discontinuities, whereas the upper and right are shock waves with a speed of  $-0.66525606186639$  only for the ideal EOS. In this test, the EOS (15) will also be considered, and the maximal value of the fluid velocity becomes very close to the speed of light as the time increases.

Figure 9 displays the contours of the density logarithm  $\ln \rho$  obtained by using PCPMSCDGP2. The interaction of four initial discontinuities leads to the distortion of the initial shock waves and the formation of a “mushroom cloud” starting from the point  $(0, 0)$  and expanding to the left bottom region. The present methods have good performance and robustness in simulating such ultra-relativistic flow. The flow structures of “mushroom cloud” for the ideal EOS (14) and EOS (15) are obviously different, and the former agrees well with that given in Wu & Tang (2015) by high-order accurate PCP finite difference WENO schemes.

**Example 5.7 (Relativistic jets).** The last 2D example is to simulate two high-speed relativistic jet flows. Jet flows with high speed are ubiquitous in the extragalactic radio sources associated with the active galactic nuclei, and the most compelling case for a special relativistic phenomenon. It is

very challenging to simulate such jet flows because strong relativistic shock waves, shear waves, interface instabilities, and ultra-relativistic regions, etc., may appear, as well as high-speed jets, (e.g., Duncan & Hughes 1994; Martí et al. 1994, 1997; Komissarov & Falle 1998; Zhang & Macfadyen 2006).

The first test is a pressure-matched hot jet model, in which the beam is moving at a speed  $v_b$ , the classical beam Mach number  $M_b$  is near the minimum Mach number for given  $v_b$ , and the relativistic effects from large beam internal energies are important and comparable to the effects from the fluid velocity near the speed of light. Initially, the computational domain  $[0, 12] \times [0, 30]$  is filled with a static uniform medium with a unit rest-mass density. A light relativistic jet is injected in the  $y$ -direction through the inlet part ( $|x| \leq 0.5$ ) on the bottom boundary ( $y = 0$ ) with a density of 0.01, a pressure equal to the ambient pressure, and a speed of  $v_b$ . The reflecting boundary condition is specified at  $x = 0$ , the fixed inflow beam condition is specified on the nozzle  $\{y = 0, |x| \leq 0.5\}$ , whereas the outflow boundary conditions are on other boundaries. The EOS is taken as (17), and three different configurations are considered as follows:

- (i)  $v_b = 0.99$  and  $M_b = 1.72$ , corresponding to the case of Lorentz factor  $W \approx 7.09$  and relativistic Mach number



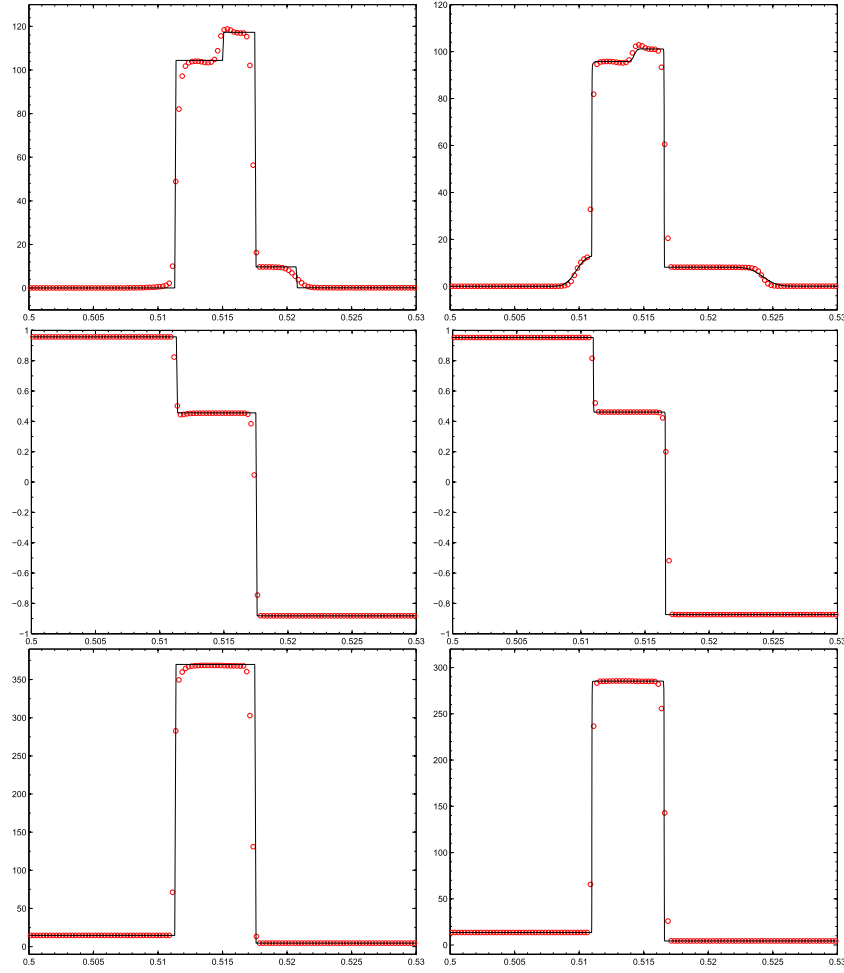
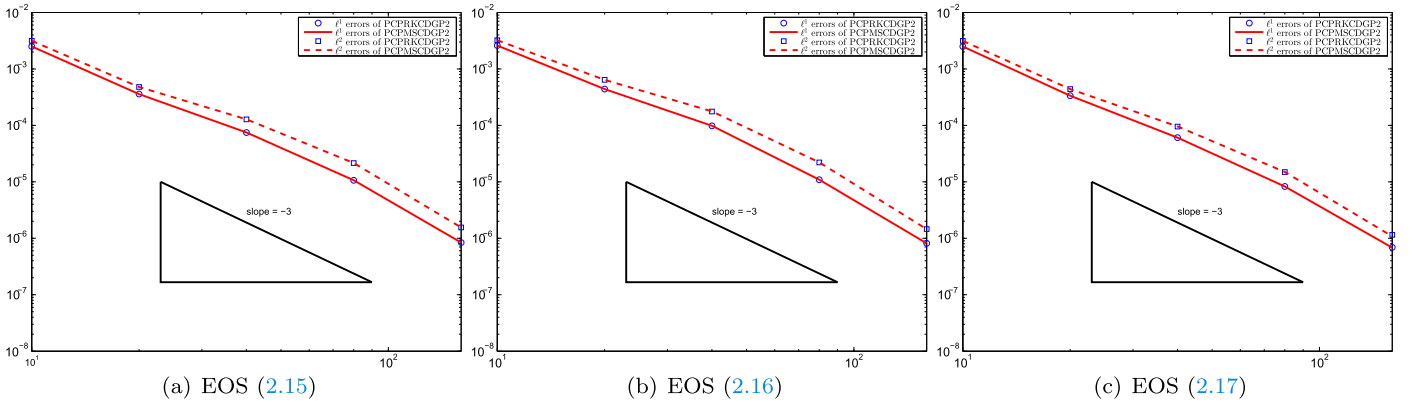


Figure 6. Same as Figure 5, except for locally using the WENO limiter.

Figure 7. Example 5.5: numerical  $l^1$ - and  $l^2$ -errors at  $t = 0.2$  of PCPRKCDGP2 and PCPMSCDGP2.

$M_r := M_b W / W_s \approx 9.97$ , where  $W_s = 1/\sqrt{1 - c_s^2}$  is the Lorentz factor associated with the local sound speed;

(ii)  $v_b = 0.999$  and  $M_b = 1.74$ , corresponding to the case of  $W \approx 22.37$  and  $M_r \approx 38.88$ ;

(iii)  $v_b = 0.9999$  and  $M_b = 1.74$ , corresponding to the case of  $W \approx 70.71$  and  $M_r \approx 123.03$ . As  $v_b$  becomes more close to the speed of light, the simulation of the jet becomes more challenging.

Figures 10 and 11 display, respectively, the schlieren images of rest-mass density logarithm  $\ln \rho$  and pressure logarithm  $\ln p$  within the domain  $[-12, 12] \times [0, 30]$  at  $t = 30$  obtained by using PCPMSCDGP2 on the uniform mesh of  $240 \times 600$  cells in the computational domain  $[0, 12] \times [0, 30]$ . The Mach shock wave at the jet head and the beam/cocoon interface are well captured during the whole simulation, and the proposed PCP methods exhibit good performance and robustness.

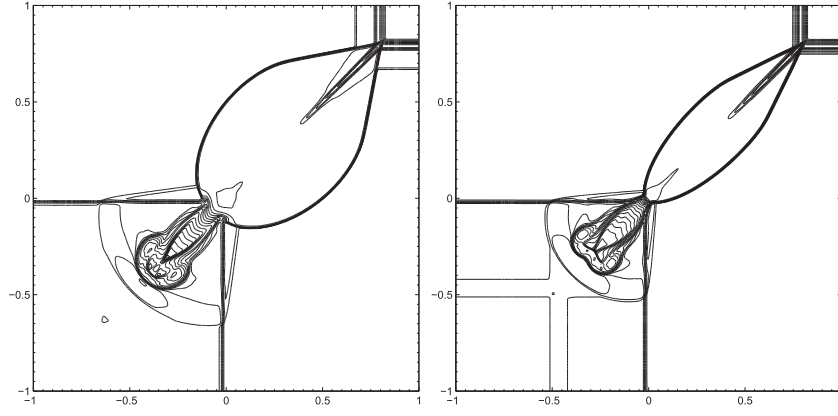


**Figure 8.** The first 2D Riemann problem in Example 5.6: the contours of density logarithm  $\ln \rho$  at  $t = 0.8$  obtained by using PCPMSCDGP2. 25 equally spaced contour lines are used. Left: ideal EOS (14) with  $\Gamma = 5/3$ ; right: EOS (16).

**Table 2**  
Example 5.5: numerical  $l^1$ - and  $l^2$ -errors and Orders at  $t = 0.2$  of PCPRKCDGP2 and PCPMSCDGP2 for the Ideal EOS with  $\Gamma = 5/3$

$N$	PCPRKCDGP2				PCPMSCDGP2			
	$l^1$ error	$l^1$ order	$l^2$ error	$l^2$ order	$l^1$ error	$l^1$ order	$l^2$ error	$l^2$ order
10	2.462e-3	...	3.091e-3	...	2.456e-3	...	3.083e-3	...
20	2.573e-4	3.26	3.446e-4	3.17	2.568e-4	3.26	3.442e-4	3.16
40	3.131e-5	3.04	4.261e-5	3.02	3.054e-5	3.07	4.227e-5	3.03
80	3.785e-6	3.05	5.278e-6	3.01	3.769e-6	3.02	5.276e-6	3.00
160	4.707e-7	3.01	6.594e-7	3.00	4.707e-7	3.00	6.594e-7	3.00

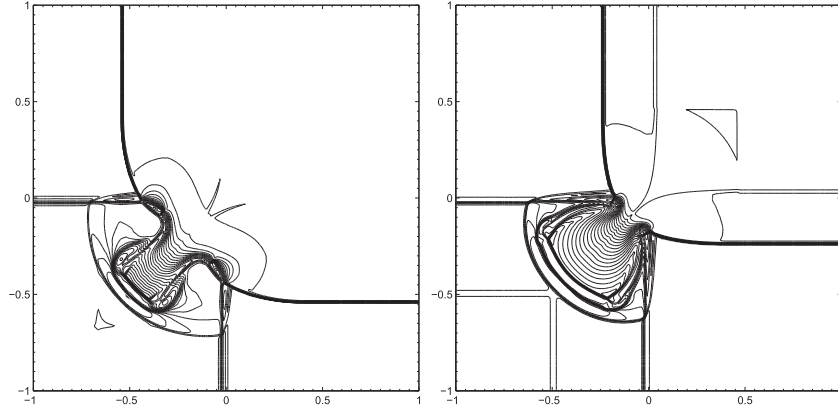


**Figure 9.** The second 2D Riemann problem in Example 5.6: the contours of density logarithm  $\ln \rho$  at  $t = 0.8$  obtained by using PCPMSCDGP2. 25 equally spaced contour lines are used. Left: ideal EOS (14) with  $\Gamma = 5/3$ ; right: EOS (15).

The second test is the pressure-matched highly supersonic jet model. The highly supersonic jet model is also referred to as the cold model, in which the relativistic effects from the large beam speed dominate, such that there exists an important difference between the hot and cold relativistic jets. The setups are the same as the above hot jet model, except for that the density of the inlet jet becomes 0.1, the EOS is taken as the ideal EOS with  $\Gamma = \frac{5}{3}$ , and the computational domain is  $[0, 12] \times [0, 25]$ . Three different configurations are considered as follows:

1. (i)  $v_b = 0.99$  and  $M_b = 50$ , corresponding to the case of Lorentz factor  $W \approx 7.09$  and relativistic Mach number  $M_r \approx 354.37$ ;

2. (ii)  $v_b = 0.999$  and  $M_b = 50$ , corresponding to the case of  $W \approx 22.37$  and  $M_r \approx 1118.09$ ;
3. (iii)  $v_b = 0.9999$  and  $M_b = 500$ , corresponding to the case of  $W \approx 70.71$  and  $M_r \approx 35356.15$ .

Figures 12 and 13 display, respectively, the schlieren images of rest-mass density logarithm  $\ln \rho$  and pressure logarithm  $\ln p$  within the domain  $[-12, 12] \times [0, 25]$ , obtained by using PCPMSCDGP2 on the uniform mesh of  $240 \times 500$  cells in the computational domain  $[0, 12] \times [0, 25]$ . The flow structures are different from those of the hot jet model, and the bow shock expands wider for larger beam velocity; our PCP central DG methods exhibit very strong robustness during the whole simulations.

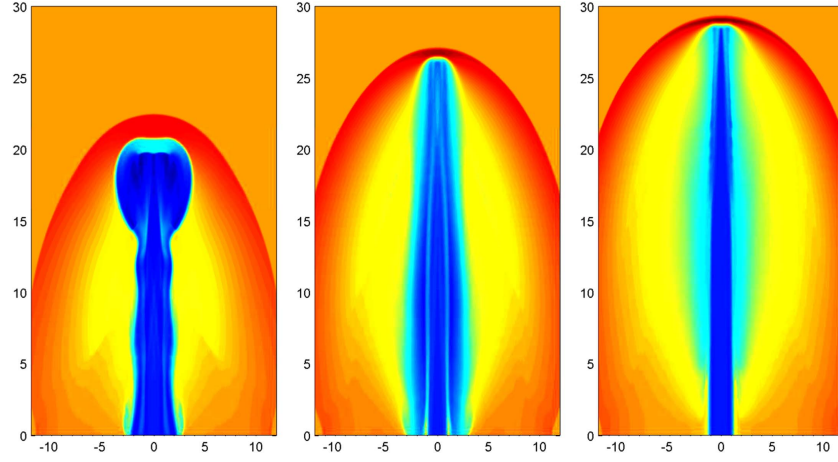


**Figure 10.** Hot jet models in Example 5.7: Schlieren images of the rest-mass density logarithm  $\ln \rho$  at  $t = 30$  obtained by PCPMSCDGP2 on the mesh of  $240 \times 600$  uniform cells. From left to right: configurations (i), (ii), and (iii).

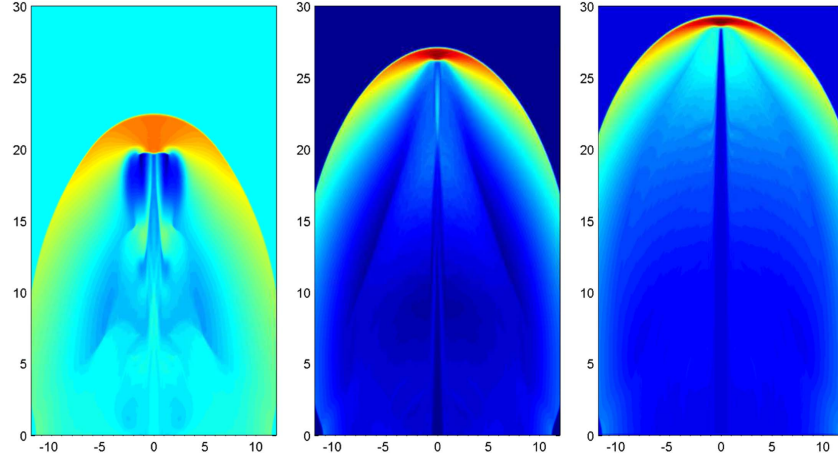


**Figure 11.** Same as Figure 10 except for the schlieren images of pressure logarithm  $\ln p$ .

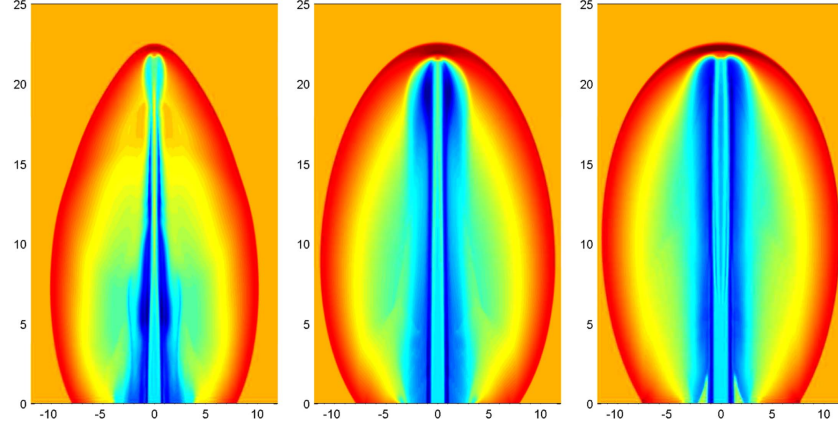


**Figure 12.** Cold jet models in Example 5.7: Schlieren images of the rest-mass density logarithm  $\ln \rho$  obtained by PCPMSCDGP2 on the uniform mesh of  $240 \times 500$  cells. From left to right: configurations (i) at  $t = 30$ , (ii) at  $t = 25$ , and (iii) at  $t = 23$ .

## 6. CONCLUSIONS

The paper developed high-order accurate PCP central DG methods for the 1D and 2D special RHD equations with a general EOS. The main contribution was proving several key properties of the admissible state set, including the convexity,

scaling and orthogonal invariance, and Lax–Friedrichs splitting property. It was done with the aid of the equivalent form of the admissible state set, and nontrivial due to the inherent nonlinearity of the RHD equations and dearth of explicit expressions of the primitive variables, as well as the flux vectors with respect to the conservative vector. Built on our

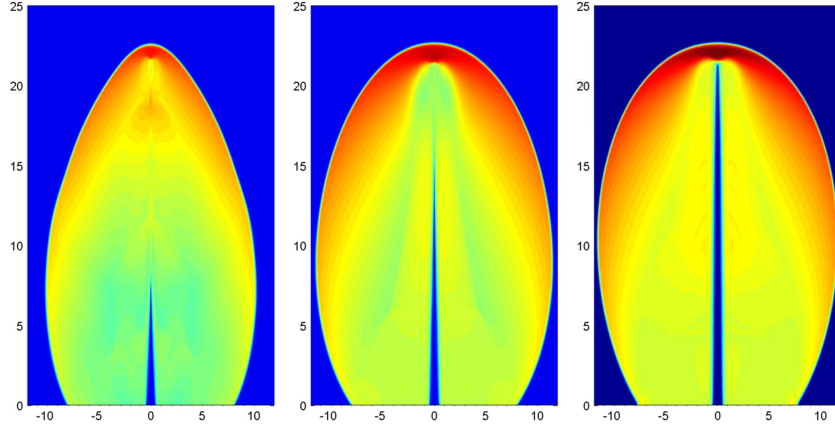


Figure 13. Same as Figure 12, except for the schlieren images of pressure logarithm  $\ln p$ .

analysis of the admissible state set, the PCP limiting procedure was designed to enforce the admissibility of the central DG solutions. The fully discrete high-order PCP central DG methods with the PCP limiting procedure and SSP time discretization were proved to preserve positivity of the density, pressure and specific internal energy and the bound of the fluid velocity under a CFL type condition, maintain high-order accuracy, and be  $L^1$ -stable. Several 1D and 2D numerical examples were used to demonstrate the accuracy, robustness, and effectiveness of the proposed PCP methods in solving several 1D and 2D relativistic fluid flow problems with large Lorentz factor, strong discontinuities, or low rest-mass density or pressure, etc. The present PCP limiting procedure and analyses could be used to develop high-order accurate PCP non-central DG, finite volume, or finite difference schemes for the RHD equations with a general EOS.

This work was partially supported by the Special Project on High-performance Computing under the National Key R&D Program (No. 2016YFB0200603), Science Challenge Project (No. JCKY2016212A502), and the National Natural Science Foundation of China (Nos. 91330205 & 11421101).

#### APPENDIX A

##### DERIVATION OF (2.6) BY THE KINETIC THEORY

Only the case of  $d = 3$  is discussed here. According to the kinetic theory (Cercignani & Kremer 2002; Rezzolla & Zanotti 2013), one has

$$D = \hat{m} \int_{\mathbb{R}^3} \hat{f} d\hat{\mathbf{p}}, \quad m_i = \int_{\mathbb{R}^3} \hat{p}^i \hat{f} d\hat{\mathbf{p}},$$

$$E = \int_{\mathbb{R}^3} \hat{p}^0 \hat{f} d\hat{\mathbf{p}}, \quad i = 1, 2, 3,$$

where  $\hat{m}$  is the rest mass of the gas particle and  $\hat{f}(t, \mathbf{x}, \hat{\mathbf{p}}) \in L^2([0, +\infty) \times \mathbb{R}^6)$  is nonnegative and denotes the equilibrium distribution function depending on the space-time and the particle momentum coordinates  $(\hat{p}^0, \hat{\mathbf{p}})$  with

$\hat{p}^0 = \sqrt{|\hat{\mathbf{p}}|^2 + \hat{m}^2}$ . It follows that

$$\begin{aligned} D^2 + |\mathbf{m}|^2 - E^2 &= \left( \hat{m} \int_{\mathbb{R}^3} \hat{f} d\hat{\mathbf{p}} \right)^2 + \sum_{i=1}^3 \left( \int_{\mathbb{R}^3} \hat{p}^i \hat{f} d\hat{\mathbf{p}} \right)^2 \\ &\quad - \left( \int_{\mathbb{R}^3} \hat{p}^0 \hat{f} d\hat{\mathbf{p}} \right)^2 \\ &\leq \left( \hat{m} \int_{\mathbb{R}^3} \hat{f} d\hat{\mathbf{p}} \right)^2 + \sum_{i=1}^3 \left( \int_{\mathbb{R}^3} |\hat{p}^i| \hat{f} d\hat{\mathbf{p}} \right)^2 - \left( \int_{\mathbb{R}^3} \hat{p}^0 \hat{f} d\hat{\mathbf{p}} \right)^2 \\ &= \left( \int_{\mathbb{R}^3} (\hat{m}^2 \hat{f}^2)^{\frac{1}{2}} d\hat{\mathbf{p}} \right)^2 + \sum_{i=1}^3 \left( \int_{\mathbb{R}^3} (|\hat{p}^i|^2 \hat{f}^2)^{\frac{1}{2}} d\hat{\mathbf{p}} \right)^2 \\ &\quad - \left( \int_{\mathbb{R}^3} \hat{p}^0 \hat{f} d\hat{\mathbf{p}} \right)^2 \\ &\leq \left( \int_{\mathbb{R}^3} \left( \hat{m}^2 \hat{f}^2 + \sum_{i=1}^3 |\hat{p}^i|^2 \hat{f}^2 \right)^{\frac{1}{2}} d\hat{\mathbf{p}} \right)^2 - \left( \int_{\mathbb{R}^3} \hat{p}^0 \hat{f} d\hat{\mathbf{p}} \right)^2 \\ &= \left( \int_{\mathbb{R}^3} \sqrt{|\hat{\mathbf{p}}|^2 + \hat{m}^2} \hat{f} d\hat{\mathbf{p}} \right)^2 - \left( \int_{\mathbb{R}^3} \hat{p}^0 \hat{f} d\hat{\mathbf{p}} \right)^2 = 0, \end{aligned} \tag{61}$$

where the reverse Minkowski inequality

$$\sum_{i=0}^3 \left( \int_{\mathbb{R}^3} (g_i(\hat{\mathbf{p}}))^{\frac{1}{2}} d\hat{\mathbf{p}} \right)^2 \leq \left( \int_{\mathbb{R}^3} \left( \sum_{i=0}^3 g_i(\hat{\mathbf{p}}) \right) d\hat{\mathbf{p}} \right)^2,$$

has been used,  $g_0 = \hat{f}^2 \hat{m}^2$ , and  $g_i = \hat{f}^2 |\hat{p}^i|^2$ ,  $i = 1, 2, 3$ .

The equal sign in (61) does not work; in other words, it always holds that  $D^2 + |\mathbf{m}|^2 < E^2$ . Otherwise, one has that (i)  $\hat{f}$  is equal to zero in the  $\hat{\mathbf{p}}$  space almost everywhere for  $\hat{\mathbf{p}}$ , or (ii) there exist three nonnegative real numbers  $\{a_i\}_{i=1}^3$  independent of  $\hat{\mathbf{p}}$ , such that

$$g_0 - a_i g_i = 0, \quad i = 1, 2, 3. \tag{62}$$

for almost  $\hat{\mathbf{p}} \in \mathbb{R}^3$ . Case (i) conflicts with the fact that

$$\int_{\mathbb{R}^3} \hat{f}(t, \mathbf{x}, \hat{\mathbf{p}}) d\hat{\mathbf{p}} = D/\hat{m} > 0,$$

whereas case (ii) also implies that  $\hat{f}$  is equal to zero almost everywhere for  $\hat{p}$  such that the same contradiction is met. In fact, if  $\hat{f}(t, \mathbf{x}, \hat{p}) \neq 0$  for fixed  $t$  and  $\mathbf{x}$ , then using (62) gives  $|\hat{p}^i| = \frac{\hat{m}}{a_i}$ , where  $a_i \neq 0$  because  $g_0 > 0$  and (62). It implies that, for fixed  $t$  and  $\mathbf{x}$ ,  $\hat{f}(t, \mathbf{x}, \hat{p}) \neq 0$  only when  $\hat{p} = (\pm \hat{m}/a_1, \pm \hat{m}/a_2, \pm \hat{m}/a_3)$ , and thus  $\hat{f}(t, \mathbf{x}, \hat{p})$  is equal to zero in the  $\hat{p}$  space almost everywhere.

For any  $\rho, p \in \mathbb{R}^+$  and  $\mathbf{v} \in \mathbb{R}^3$  satisfying  $v = |\mathbf{v}| < 1$ , it holds that

$$0 < E^2 - (D^2 + |\mathbf{m}|^2) = \frac{1}{1 - v^2} [\rho^2(1 + e)^2 - \rho^2 - p^2 v^2].$$

The arbitrary of  $\mathbf{v} \in \mathbb{R}^3$  with  $v < 1$  yields

$$\inf_{v < 1} (\rho^2(1 + e)^2 - \rho^2 - p^2 v^2) \geq 0.$$

Thus, one has  $\rho^2(1 + e(p, \rho))^2 - \rho^2 - p^2 \geq 0$ , which is verified as equivalent to (6) by noting  $e > 0$  and (3).

## REFERENCES

- Biswas, R., Devine, K., & Flaherty, J. E. 1994, *ApNM*, 14, 255
- Blandford, R. D., & McKee, C. F. 1976, *PhFI*, 19, 1130
- Cercignani, C., & Kremer, G. M. 2002, *The Relativistic Boltzmann Equation: Theory and Applications* (Basel: Birkhäuser)
- Cheng, Y., Li, F. Y., Qiu, J. X., & Xu, L. W. 2013, *JCoPh*, 238, 255
- Choi, E., & Wiita, P. J. 2010, *ApJS*, 191, 113
- Christlieb, A. J., Liu, Y., Tang, Q., & Xu, Z. F. 2015, *SIAM J. Sci. Comput.*, 37, A1825
- Cockburn, B., Hu, S. C., & Shu, C.-W. 1990, *MaCom*, 54, 545
- Cockburn, B., Lin, S. Y., & Shu, C.-W. 1989, *JCoPh*, 84, 90
- Cockburn, B., & Shu, C.-W. 1989, *MaCom*, 52, 411
- Duncan, G. C., & Hughes, P. A. 1994, *ApJL*, 436, L119
- Falle, S. A. E. G., & Komissarov, S. S. 1996, *MNRAS*, 278, 586
- Font, J. A. 2008, *LRR*, 11, 7
- Gottlieb, S., Ketcheson, D. J., & Shu, C.-W. 2009, *JSCom*, 38, 251
- Hu, X. Y., Adams, N. A., & Shu, C.-W. 2013, *JCoPh*, 242, 169
- Jiang, Y., & Xu, Z. F. 2013, *SIAM J. Sci. Comput.*, 35, A2524
- Komissarov, S. S., & Falle, S. A. E. G. 1998, *MNRAS*, 297, 1087
- Landau, L. D., & Lifshitz, E. M. 1987, *Fluid Mechanics* (Oxford: Pergamon Press)
- Li, F. Y., & Xu, L. W. 2012, *JCoPh*, 231, 2655
- Li, F. Y., Xu, L. W., & Yakovlev, S. 2011, *JCoPh*, 230, 4828
- Li, F. Y., & Yakovlev, S. 2010, *JSCom*, 45, 404
- Liang, C., & Xu, Z. F. 2014, *JSCom*, 58, 41
- Liu, Y. J., Shu, C.-W., Tadmor, E., & Zhang, M. P. 2007, *SINUM*, 45, 2442
- Liu, Y. J., Shu, C.-W., Tadmor, E., & Zhang, M. P. 2008, *ESAIM Math. Model. Numer. Anal.*, 42, 593
- Lucas-Serrano, A., Font, J. A., Ibáñez, J. M., & Martí, J. M. 2004, *A&A*, 428, 703
- Martí, J. M., & Müller, E. 1994, *JFM*, 258, 317
- Martí, J. M., & Müller, E. 1996, *JCoPh*, 123, 1
- Martí, J. M., & Müller, E. 2003, *LRR*, 6, 7
- Martí, J. M., Müller, E., Font, J. A., Ibáñez, J. M., & Marquina, A. 1997, *ApJ*, 479, 151
- Martí, J. M., Müller, E., & Ibáñez, J. M. 1994, *A&A*, 281, L9
- Mathews, W. G. 1971, *ApJ*, 165, 147
- May, M. M., & White, R. H. 1966, *PhRv*, 141, 1232
- May, M. M., & White, R. H. 1967, in *Methods in Computational Physics*, Vol. 7, ed. B. Alder, S. Fernbach, & M. Rotenberg (New York: Academic), 219
- Mignone, A., Plewa, T., & Bodo, G. 2005, *ApJS*, 160, 199
- Qin, T., Shu, C.-W., & Yang, Y. 2016, *JCoPh*, 315, 323
- Qiu, J. X., & Shu, C.-W. 2005, *SIAM J. Sci. Comput.*, 26, 907
- Rezzolla, L., & Zanotti, O. 2013, *Relativistic Hydrodynamics* (Oxford: Oxford Univ. Press)
- Ryu, D., Chattopadhyay, I., & Choi, E. 2006, *ApJS*, 166, 410
- Sokolov, I. V., Zhang, H.-M., & Sakai, J. I. 2001, *JCoPh*, 172, 209
- Synge, J. L. 1957, *The Relativistic Gas* (Amsterdam: North-Holland)
- Taub, A. H. 1948, *PhRv*, 74, 328
- Wang, C., Zhang, X. X., Shu, C.-W., & Ning, J. G. 2012, *JCoPh*, 231, 653
- Wilson, J. R. 1972, *ApJ*, 173, 431
- Wu, K. L., & Tang, H. Z. 2014, *JCoPh*, 256, 277
- Wu, K. L., & Tang, H. Z. 2015, *JCoPh*, 298, 539
- Wu, K. L., & Tang, H. Z. 2016, arXiv:1603.06660
- Wu, K. L., & Tang, H. Z. 2016, *SIAM J. Sci. Comput.*, 38, B458
- Xing, Y. L., Zhang, X. X., & Shu, C.-W. 2010, *AdWR*, 33, 1476
- Xiong, T., Qiu, J.-M., & Xu, Z. F. 2016, *JSCom*, 67, 1066
- Xu, Z. F. 2014, *MaCom*, 83, 2213
- Xu, Z. F., & Zhang, X. X. 2016, *Handbook on Numerical Methods for Hyperbolic Problems* (Amsterdam: North-Holland, Elsevier) submitted. Available at <https://www.math.purdue.edu/~zhan1966/research/>
- Yakovlev, S., Xu, L. W., & Li, F. Y. 2013, *JComS*, 4, 80
- Yang, Z. C., He, P., & Tang, H. Z. 2011, *JCoPh*, 230, 7964
- Zanna, L. D., & Bucciantini, N. 2002, *A&A*, 390, 1177
- Zhang, W. Q., & Macfadyen, A. I. 2006, *ApJS*, 164, 255
- Zhang, X. X., & Shu, C.-W. 2010a, *JCoPh*, 229, 3091
- Zhang, X. X., & Shu, C.-W. 2010b, *JCoPh*, 229, 8918
- Zhang, X. X., & Shu, C.-W. 2011a, *JCoPh*, 230, 1238
- Zhang, X. X., & Shu, C.-W. 2011b, *RSPSA*, 467, 2752
- Zhang, X. X., Xia, Y. H., & Shu, C.-W. 2012, *JSCom*, 50, 29
- Zhao, J. 2014, PhD thesis, School of Mathematical Sciences, Peking Univ.
- Zhao, J., & Tang, H. Z. 2013, *JCoPh*, 242, 138
- Zhao, J., & Tang, H. Z. 2016a, arXiv:1609.06792
- Zhao, J., & Tang, H. Z. 2016b, arXiv:1610.03404
- Zhu, J., Qiu, J. X., Shu, C.-W., & Dumbser, M. 2008, *JCoPh*, 227, 4330